Official Journal of Turkish Society of Magnetic Resonance

CRMRI

Current Research in MRI

Diagnostic Efficacy of Multiparametric Magnetic Resonance Imaging Parameters in Differentiating Common Subtypes of Renal Cortical Tumors

İsmet Miraç Çakır, Tümay Bekçi, Uluhan Eryuruk, Nisa Baspinar, Serdar Aslan

Cutis Verticis Gyrata: A Rare Finding in Cranial Magnetic Resonance Imaging that Is Usually Overlooked

Derya Güçlü, Osman Şinasi Oğuz, Hayri Oğul

The Role of 3 Tesla Diffusion Weighted-Magnetic Resonance Imaging and Apparent Diffusion Coefficient Mapping with Aging and Gendering in Primary Parotid Tumors: Preoperative Foresight of Histopathological Subtypes

Abdurrahim Dusak, Adem Ağyar, Mustafa Çelik, Saime Shermatova, Veysel Kaya, Muhammed Emin Güldür

Correlation of Qualitative and Quantitative Characteristics of Contrast-Enhanced Dynamic Magnetic Resonance Imaging with Hepatospecific Contrast Agent Gadoxetic Acid (Primovist) and Histopathological Differentiations in Hepatocellular Carcinoma

Kairgeldy Aikimbaev, Hüseyin Tuğsan Ballı, Kıvılcım Eren Erdoğan, Yusuf Can, Ferhat Can Pişkin, Sinan Sözütok, Şükrü Mehmet Ertürk

Magnetic Resonance Measurement of Lateral Ventricular Diameters in Cases of Colpocephaly and Corpus Callosum Agenesis

Önder Durmaz, Erdem Fatihoğlu, Ali Osman Gülmez

AVES

curremr.com

TMRD
TÜRK MANYETİK
REZONANS DERNEĞİ
TURKISH SOCIETY
OF MAGNETIC RESONANCE

Current Research in MRI

TMRD
TÜRK MANYETİK
REZONANS DERNEĞİ
TURKISH SOCIETY
OF MAGNETIC RESONANCE

Current Research in MRI

AIMS AND SCOPE

Current Research in MRI (Curr Res MRI) is a scientific, open access, online-only official publication of the Turkish Society of Magnetic Resonance published in accordance with independent, unbiased, and double-blinded peer-review principles. The journal is published triannually in April, August, and December. The publication language of the journal is English.

Current Research in MRI aims to contribute to the literature by publishing manuscripts at the highest scientific level on radiology. The journal publishes original articles, reviews, case reports, and letters to the editor that are prepared in accordance with ethical guidelines.

The target audience of the journal includes specialists, researchers and professionals who working and interested in the field of radiology.

The editorial and publication processes of the journal are shaped in accordance with the guidelines of the International Committee of Medical Journal Editors (ICMJE), World Association of Medical Editors (WAME), Council of Science Editors (CSE), Committee on Publication Ethics (COPE), European Association of Science Editors (EASE), and National Information Standards Organization (NISO). The journal is in conformity with the Principles of Transparency and Best Practice in Scholarly Publishing (doaj.org/bestpractice).

Publication Fee Policy

All expenses of the journal are covered by the Turkish Society of Magnetic Resonance. Processing and publication are free of charge with the journal. No fees are requested from the authors at any point throughout the evaluation and publication process. All manuscripts must be submitted via the online submission system, which is available at http://curremr.com. The journal guidelines, technical information, and the required forms are available on the journal's web page.

Advertisement Policy

Current Research in MRI can publish advertisement images in the journal's website upon the approval of the Editor in Chief. Potential advertisers should contact the Editorial Office. Advertisers have no effect on the editorial decisions or advertising policies.

Disclaimer

Statements or opinions expressed in the manuscripts published in the journal reflect the views of the author(s) and not the opinions of the editors, editorial board, and/or publisher; the editors, editorial board, and publisher disclaim any responsibility or liability for such materials.

Open Access Statement

Current Research in MRI is an open access publication, and the journal's publication model is based on Budapest Access Initiative (BOAI) declaration. All published content is available online, free of charge at http://curremr.com. The journal's content is licensed under a Creative Commons Attribution-NonCommercial (CC BY-NC) 4.0 International License which permits third parties to share and adapt the content for non-commercial purposes by giving the appropriate credit to the original work.

You can reach the current version of the instructions to authors at https://curremr.com/EN

Current Research in MRI

CONTENTS

Diagnostic Efficacy of Multiparametric Magnetic Resonance Imaging Parameters in Differentiating Common Subtypes of Renal Cortical Tumors

İsmet Miraç Çakır[1], Tümay Bekçi[1], Uluhan Eryuruk[1], Nisa Baspinar[2], Serdar Aslan[1]

[1]Department of Radiology, Giresun University, Faculty of Medicine, Giresun, Turkey
[2]Department of Radiology, Cumhuriyet University, Faculty of Medicine, Sivas, Turkey

Abstract

Objective: The purpose of study was to assess the diagnostic efficacy of multiparametric magnetic resonance imaging in differentiating common subtypes of renal cortical tumors.

Methods: The study group was formed with 85 renal cortical tumors of 75 patients who underwent surgery for renal mass and who had preoperative multiparametric magnetic resonance imaging. Two radiologists were blinded to pathology results evaluated using T2-weighted images, apparent diffusion coefficient maps, and dynamic contrast-enhanced T1-weighted images. T2 signal intensity ratio, apparent diffusion coefficient ratio, corticomedullary phase enhancement ratio, nephrogenic phase enhancement ratio, and delayed phase enhancement ratio were calculated for each tumor type.

Results: Between clear cell renal cell carcinomas and papillary renal cell carcinomas, T2 signal intensity ratio, corticomedullary phase enhancement ratio, nephrogenic phase enhancement ratio, and apparent diffusion coefficient ratio were statistically significantly different ($P < .001$, $P < .001$, $P = .003$, $P = .03$, respectively). Also, there was a significant difference in corticomedullary phase enhancement ratio between clear cell renal cell carcinomas and chromophobe renal cell carcinoma ($P = .031$). Between papillary renal cell carcinomas and chromophobe renal cell carcinomas, T2 signal intensity ratio ($P < .001$), corticomedullary phase enhancement ratio ($P < .001$), nephrogenic phase enhancement ratio ($P = .007$), delayed phase enhancement ratio ($P = .004$), and apparent diffusion coefficient ratio ($P < .001$) were statistically significantly different. Nephrogenic phase enhancement ratio and delayed phase enhancement ratio showed a significant difference between chromophobe renal cell carcinomas and oncoctyomas ($P = .038$ and $P = .032$, respectively). The most efficient parameter in distinguishing clear cell renal cell carcinoma was corticomedullary phase enhancement ratio, and the sensitivity was 80.4% and the specificity was 73.5% with a cutoff value of 283.6.

Conclusion: We think that the use of multiparametric magnetic resonance imaging quantitative parameters was useful in differentiating subtypes of renal cortical tumors.

Keywords: Diffusion-weighted imaging, magnetic resonance imaging, oncocytomas, renal cell carcinomas, renal cortical tumors

INTRODUCTION

Renal cell carcinoma (RCC) is the most frequent renal malignancy in adults and has 3 main subtypes: clear (75%), papillary (10%-15%), and chromophobe (5%) forms.[1,2] Prognosis of papillary and chromophobe subtypes is better than clear cell RCCs.[3] Oncocytomas compose 3%-7% of solid renal tumors and are known to be benign neoplasms. Oncocytomas have similar origin as chromophobe RCCs and therefore have convergent histological and imaging features.[4]

The histopathology of approximately 10%-30% of renal tumors excised surgically is benign.[5,6] In order to avoid unnecessary surgical operations, an image-guided biopsy is recommended before treatment; however, its use remains controversial as it is invasive and not time efficient.[7-9] In elderly or inoperative patients, treatment predilections such as active surveillance and focal ablation are used as an alternative to surgery in clinical practice. The presence of less invasive alternative treatment methods has led to a clinical need for accurate recognition of renal lesions before treatment to avoid potentially inadequate treatment.[10] Multiparametric magnetic resonance imaging (mpMRI) established on various anatomic and functional parameters have an important role and add diagnostic value in the detection and differentiation of renal cortical tumors.[11] Magnetic resonance imaging may be beneficial in distinguishing benign solid renal masses from some RCC subtypes and foreseeing the histologic grade of a tumor and play a crucial role in ensuring appropriate patient management to avoid unnecessary surgery or other interventions.

The purpose of this study was to assess the diagnostic efficacy of mpMRI differentiating frequent subtypes of renal cortical tumors.

METHODS

Patient Group

This single-institution, retrospective study was approved by the institutional ethics committee, and informed consent was waived (ethics committee number: 11484, date: September 25, 2022). In our study, the hospital database images of patients older than 18 years who had partial or radical nephrectomy surgery because of malignant renal masses between May 2018 and January 2022 were scanned retrospectively. Preoperative abdominal MRIs were performed in 98 of the patients. As the pathology results of 8 of the 98 patients could not be accessed, and the MRI examination of 5 patients was carried out without a contrast agent, these patients were excluded from the study. Three patients with histopathological results compatible with angiomyolipoma (AML) and 7 patients with rare forms of RCCs (multilocular, cystic carcinoma, tubulocystic renal cell carcinoma, and papillary adenoma) were excluded. Seventy-five patients overall with 85 renal cortical tumors were included in the study, with 1 patient having bilateral and 5 patients having multifocal renal cortical tumors. Fifty-one of tumors

> ### MAIN POINTS
>
> - Multiparametric magnetic resonance imaging plays a crucial role and adds diagnostic value in the detection and differentiation of the renal cortical tumors.
> - Corticomedullary phase enhancement ratio is the most effective parameter in distinguishing clear cell renal cell carcinomas with an accuracy of 77.7%.
> - Multiparametric magnetic resonance imaging can be used to recognize non-clear cell renal cell carcinomas in patients at high medical risk for interventional procedures or surgery and to encourage active surveillance in appropriate patients.

were reported as clear cell carcinoma, 16 were reported as papillary cell carcinoma, 8 were reported as chromophobe cell carcinoma, and 10 as oncocytoma. The study flow chart is shown in Figure 1.

Magnetic Resonance Imaging Protocol

All MRI examinations were carried out on the same 1.5-T MRI system (Magnetom Symphony; Siemens Medical Solutions, Erlangen, Germany) with a phased-array body coil. The MRI protocol comprised of the following sequences: turbo-spin echo T2-weighted images (T2WI); axial T2WI with fat suppression (FS); axial gradient-echo T1-weighted images (T1WI) with and without FS; axial diffusion-weighted images (DWIs) with b-values of 0, 400, and 800 s/mm^2. Three-dimensional axial T1WI images with FS were obtained both before and after contrast agent. Gadopentetate dimeglumine (Gadovist, Bayer Healthcare, Berlin, Germany) was administered at a dose of 0.1 mL/kg with an injection rate of 3 mL/s, followed by a 10 mL of normal saline infusion. After intravenous gadolinium injection, dynamic contrast enhanced (DCE) images were performed in 3 post-contrast phases, each with a delay of 30 s.

Magnetic Resonance Imaging Evaluation

Magnetic resonance images of 85 renal masses included in the study were estimated retrospectively by 2 radiologists (reader 1 with 11 years of abdominal radiology practice and reader 2 with 10 years), independently of histopathological results. All MRI images were uploaded to a picture archiving communication system. While evaluating T2WI, apparent diffusion coefficient (ADC) maps, and DCE–T1WI, a circular region of interest (ROI) was placed in the tumor and normal cortex parenchyma. The mean ROI size used was 100 mm^2.

T2 measurements were evaluated from both the tumor and non-tumor normal renal cortex. Region of interest measurements were taken from
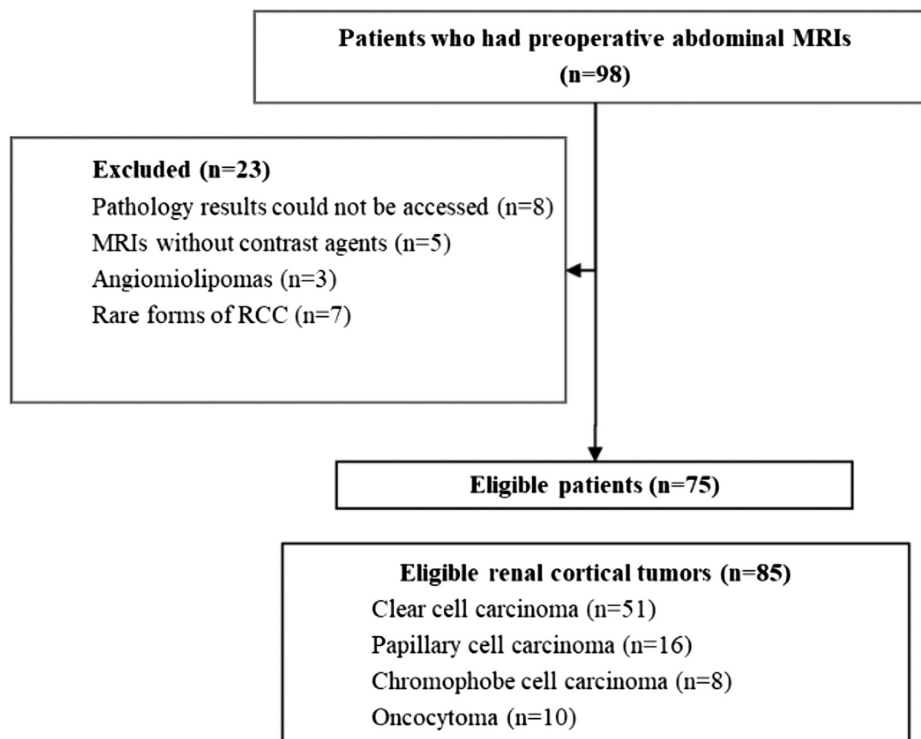

Figure 1. Study flowchart. MRI, magnetic resonance imaging; RCC, renal cell carcinoma.

3 different points in the solid areas of the tumor without necrosis, and the mean value of these measurements was recorded. This measurement was also carried out similar to the normal non-tumor renal cortical area. T2 signal intensity ratio (T2SIR) (tumor (Tu) SI/normal renal cortex (C) SI) × 100 was calculated from the measurements taken from the tumor and normal renal cortex.

In the DCE images, a single ROI was placed over the solid enhancing region without necrosis avoiding vascular structures, cystic components of the tumor, and retroperitoneal adipose tissue in the corticomedullary phase. The tumor enhancement ratio (ER) was calculated from the corticomedullary, nephrogenic, and excretory phases. The ER was calculated as [(post-contrast SI – pre-contrast SI)/pre-contrast SI] × 100. Three ERs were calculated based on the post-contrast phase: an ERc using corticomedullary phase, an ERn using the nephrogenic phase, and an ERd using the delayed phase.

Apparent diffusion coefficient measurements were taken from both the tumor and non-tumor normal renal cortex. Considering T2W and DCE images, ROI measurements were taken from 3 different points in the solid areas of the tumor without necrosis, and the mean value of these measurements was recorded. This measurement was also carried out similar to the normal non-tumor renal cortical area. The ADC ratio (ADCr) (tumor ADC/normal renal cortex ADC) × 100 was calculated from the measurements taken from the tumor and normal renal cortex.

All quantitative parameters were calculated independently by 2 readers. Disputes among readers were resolved by consulting a radiologist with 12 years of abdominal radiology experience.

Statistical Analysis
IBM Statistical Package for Social Sciences version 25.0 (IBM SPSS Corp.; Armonk, NY, USA) statistical analysis software was used in the analysis of the data. Shapiro–Wilk test was used to evaluate the normality of quantitative data distribution. The Mann–Whitney U test and Kruskal–Wallis test were used to compare quantitative data that did not exhibit normal distribution. The Bonferroni correction was carried out

Table 1. Quantitative Parameters for Common Renal Cortical Tumor Types

	Clear Cell RCC	Papillary RCC	Chromophobe RCC	Oncocytoma
T2SIR				
R1	129.3 ± 34.7	84.2 ± 17.3	121.2 ± 11.7	140.7 ± 36.1
R2	133.5 ± 44.2	95.3 ± 26.3	114.4 ± 10.2	174.2 ± 44.2
ERc				
R1	332.5 ± 62.2	182.3 ± 38.5	248.6 ± 52.1	319.3 ± 47.9
R2	310.2 ± 48.2	188.1 ± 42.2	233.5 ± 49.4	308.4 ± 42.5
ERn				
R1	316.9 ± 63.9	247.7 ± 56.9	244.4 ± 50.1	360.7 ± 103.1
R2	322.4 ± 72.4	259.5 ± 61.3	249.5 ± 53.4	369.1 ± 112.3
ERd				
R1	302.8 ± 67.1	260.9 ± 46.6	241.2 ± 49.4	371.6 ± 125.8
R2	314.8 ± 71.7	271.3 ± 55.9	249.6 ± 55.2	383.2 ± 133.4
ADCr				
R1	92.4 ± 15.9	60.4 ± 21.4	85.5 ± 12.8	108 ± 27.6
R2	96.3 ± 17.2	58.4 ± 19.2	89.6 ± 13.4	101 ± 26.7

ADCr, apparent diffusion coefficient ratio; ERc, corticomedullary phase enhancement ratio; ERd, delayed phase enhancement ratio; ERn, nephrogenic phase enhancement ratio; R1, reader 1; R2, reader 2; RCC, renal cell carcinoma; T2SIR, T2 signal intensity ratio.

for the comparison of more than 2 groups. A receiver operating characteristic analysis was used to determine the cutoff values of radiological parameters for the prediction of the pathologically diagnosed clear cell RCC. Therefore, the area under the curve, sensitivity, and specificity values were calculated. Data were presented as mean ± SD and n (%). P values of <.05 were considered statistically significant.

RESULTS
Patient Demographics and Renal Tumors
The mean age of the patients was 56.7 ± 11.5 years (range: 18-85). Thirty-three (38.8%) of the patients were female and 52 (61.2%) were male. The mean tumor size was 45.6 mm (median: 40, range: 8-127) for clear cell RCCs, 36.5 mm (median: 29.5, range: 11-98) for papillary RCCs, 62.8 mm (median: 76, range: 18-114) for chromophobe RCCs,

Figure 2. Clear cell renal cell carcinoma in the right kidney of a 63-year-old man. (A) Axial T2-weighted magnetic resonance (MR) image shows the renal mass with high signal intensity compared with renal parenchyma (T2SIR = 109.3). A region of interest has been drawn in the solid enhancing region without necrosis avoiding vascular structures and cystic components of the tumor and then reported on all sequences. (B) Apparent diffusion coefficient (ADC) maps show slight restriction of diffusion in the renal mass (ADCr = 83.6). Axial non-enhanced (C) and contrast-enhanced T1-weighted MR images in corticomedullary (D), nephrogenic (E), and delayed (F) phases show early and intense enhancement of mass in corticomedullary phase followed by washout (ERc: 366.6 , ERn: 329.5, ERd: 321.1). ADCr, ADC ratio; ERc, corticomedullary phase enhancement ratio; ERd, delayed phase enhancement ratio; ERn, nephrogenic phase enhancement ratio.
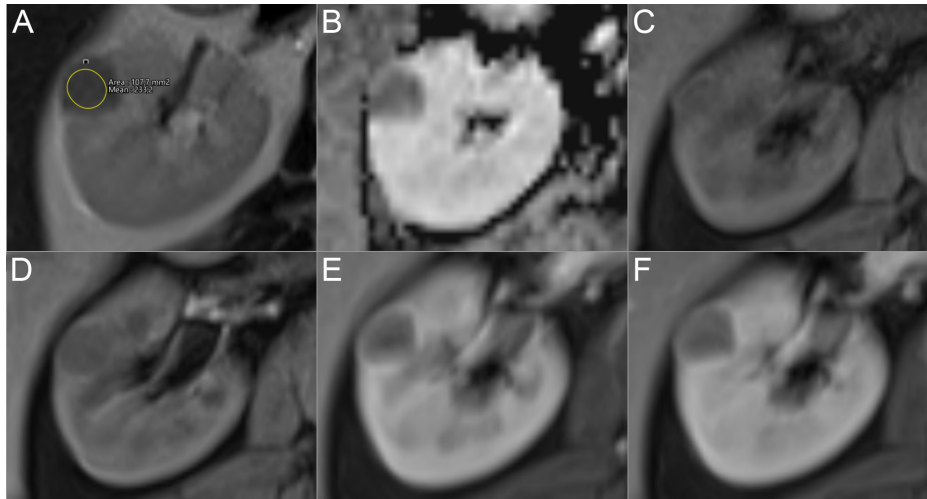
Figure 3. Papillary renal cell carcinoma in the right kidney of a 51-year-old man. (**A**) Axial T2-weighted magnetic resonance (MR) image shows significant a renal mass with low signal intensity compared to renal parenchyma (T2SIR=67). (B) Apparent diffusion coefficient (ADC) maps show markedly low ADC values in the renal mass (ADCr=44.5). Axial non-enhanced (C) and contrast-enhanced T1-weighted MR images in corticomedullary (D), nephrogenic (E), and delayed (F) phases show slowly increasing enhancement of the mass (ERc: 78.2, ERn: 93.4, ERd: 121.7). ADCr, ADC ratio; ERc, corticomedullary phase enhancement ratio; ERd, delayed phase enhancement ratio; ERn, nephrogenic phase enhancement ratio.

and 33.8 mm (median: 29, range: 18-87) for oncocytomas. There were statistically significant differences in tumor sizes between chromophobe RCCs and papillary RCCs and between chromophobe RCCs and oncocytoma ($P < .012$). No significant difference in size was observed between other tumor groups.

Multiparametric Magnetic Resonance Imaging the Quantitative Analysis of Renal Tumors
Table 1 presents the results of 2 readers for all the evaluated MRI parameters.

Interobserver agreement was almost perfect, with weighted K values ranging from 0.89 to 0.93 in the calculation of MRI quantitative parameters.

There was a statistically significant difference between papillary RCCs and the other renal cortical tumors in T2SIR ($P < .001$).

Considering the post-contrast dynamic behavior, there was a statistically significant difference between clear cell RCCs (Figure 2) and papillary RCCs (Figure 3), clear cell RCCs and chromophobe RCC (Figure 4), and papillary RCC and oncocytoma (Figure 5) in ERc ($P < .001$, $P=.031$ and $P < .001$, respectively). There was a statistically significant difference between clear cell RCC and papillary RCC, chromophobe RCC and oncocytoma, and papillary RCC and oncocytoma in ERn ($P=.004$, $P=.038$ and $P=.007$, respectively). There was a statistically significant difference between chromophobe RCC and oncocytoma and between papillary RCC and oncocytoma in ERd ($P=.040$ and $P=.031$, respectively) (Table 2).
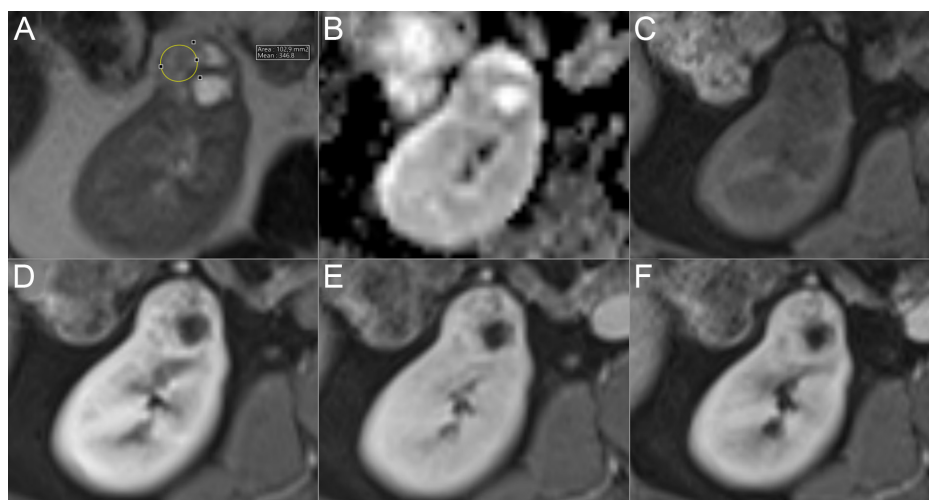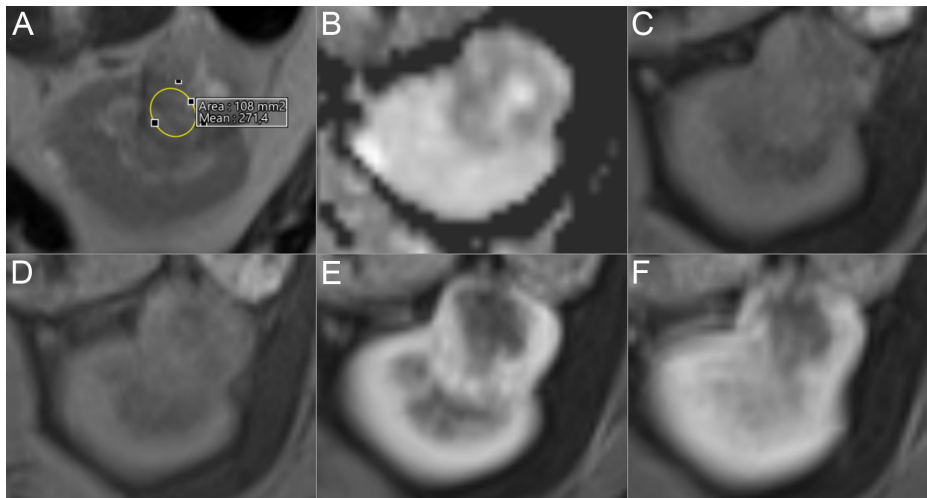

Figure 4. Chromophobe renal cell carcinoma in the left kidney of a 39-year-old man. (A) Axial T2-weighted magnetic resonance (MR) image shows a renal mass with almost the same signal intensity compared to renal parenchyma (T2SIR=98). (B). Apparent diffusion coefficient (ADC) maps show diffusion restriction in the solid areas of renal mass (ADCr=59.5). Axial non-enhanced (C) and contrast-enhanced T1-weighted MR images in corticomedullary (D), nephrogenic (E), and delayed (F) phases show moderate enhancement of the mass without washout (ERc: 122.6, ERn: 126.6, ERd: 128). ADCr, ADC ratio; ERc, corticomedullary phase enhancement ratio; ERd, delayed phase enhancement ratio; ERn, nephrogenic phase enhancement ratio.
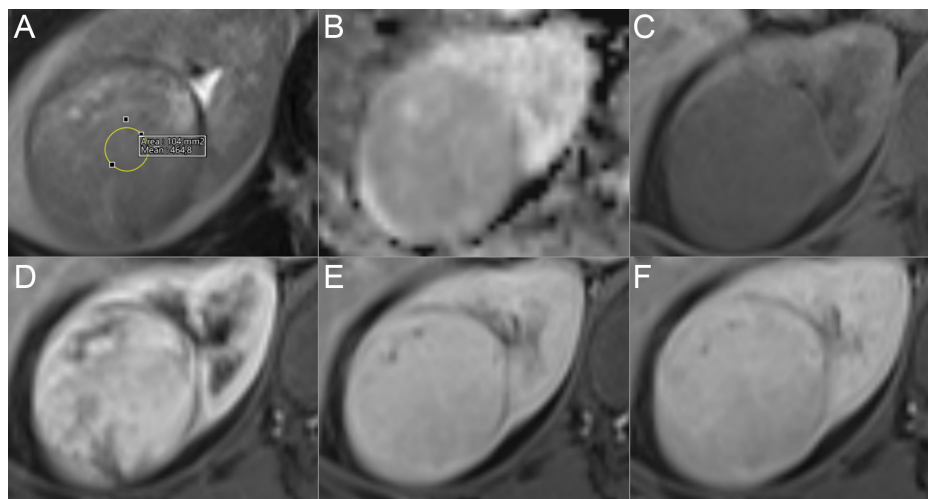
Figure 5. Oncocytoma in the right kidney of a 41-year-old man. (A) Axial T2-weighted magnetic resonance image shows a renal mass with slightly high SI compared to renal parenchyma (T2SIR=116). (B) Apparent diffusion coefficient (ADC) maps show diffusion restriction in the renal mass (ADCr=75). Axial non-enhanced (C) and contrast-enhanced T1-weighted MR images in corticomedullary (D), nephrogenic (E), and delayed (F) phases show strong heterogenous enhancement of mass in corticomedullary followed by washout (ERc: 281.9, ERn: 259, ERd: 250.4). ADCr, ADC ratio; ERc, corticomedullary phase enhancement ratio; ERd, delayed phase enhancement ratio; ERn, nephrogenic phase enhancement ratio.

There was a statistically significant difference in ADCr between clear cell RCC and papillary RCC, and between papillary RCC and oncocytoma ($P < .001$).

Recognition of Clear Cell Renal Cell Carcinoma

The most efficient parameters in discriminating clear cell RCC from other renal cortical tumors were ERc and T2SIR (Table 3). Between the 2 tumor groups, sensitivity was 80.4% and specificity was 73.5% in ERc with a cutoff value of 283.6 and sensitivity was 78.4% and specificity 70.6% in T2SIR with a cutoff value of 107.2 (Figure 6).

DISCUSSION

In our study, T2 signal ratios, ADCr, and ER parameters obtained from mpMRI examination had high diagnostic accuracy in differentiating common subtypes of renal cortical tumors.

Each subtype of renal cortical tumors has different T2 signal properties as they have different histological, morphological, and genetic characteristics. Clear cell RCCs tend to be hyperintense on T2WI due to necrosis and/or cystic degeneration. Papillary cell RCCs are usually hypointense on T2WI due to hemosiderin deposition.[12,13] Whereas, chromophobe RCCs tend to have moderate-to-low T2 signals. T2 signals of oncocytomas are usually high compared to the renal cortex,

Table 2. Statistically Significant *P* Values of the Quantitative Characteristics Between Each Renal Cortical Tumor Type

	Clear Cell RCC and Papillary RCC	Clear cell RCC and Chromophobe RCC	Clear cell RCC and Oncocytoma	Papillary RCC and Chromophobe RCC	Papillary RCC and Oncocytoma	Chromophobe RCC and Oncocytoma
T2SIR	**<.001**	1.000	1.000	**<.001**	**<.001**	1.000
ERc	**<.001**	**.031**	1.000	.639	**<.001**	.352
ERn	**.004**	.075	1.000	1.000	**.007**	**.038**
ERd	.264	.202	.813	1.000	**.040**	**.031**
ADCr	**.001**	1.000	1.000	.317	**<.001**	.424

ADCr, apparent diffusion coefficient ratio; ERc, corticomedullary phase enhancement ratio; ERd, delayed phase enhancement ratio; ERn, nephrogenic phase enhancement ratio; RCC, renal cell carcinoma; T2SIR, T2 signal intensity ratio. Statistically significant p values are in bold format.

Table 3. Results of ROC Analysis and Measures of Accuracy in Determining Clear Cell RCC

	T2SIR	ERc	ERn	ERe	ADCr
AUC	0.771 (0.662-0.881)	0.828 (0.736-0.921)	0.668 (0.543-0.793)	0.59 (0.463-0.717)	0.682 (0.55-0.814)
P	<.001	<.001	.009	.162	.005
Cutoff	107.2	283.6	291.1	283.05	80.25
Sensitivity	78.4 (64.68-88.71)	80.4 (66.88-90.18)	74.5 (60.37-85.67)	54.9 (40.34-68.87)	84.3 (71.41-92.98)
Specificity	70.6 (52.52-84.9)	73.5 (55.64-87.12)	61.8 (43.56-77.83)	52.9 (35.13-70.22)	58.8 (40.7-75.35)
PPV	80 (69.97-87.29)	82 (71.91-89.02)	74.5 (64.94-82.19)	63.6 (53.12-72.99)	75.4 (66.89-82.36)
NPV	68.6 (55.32-79.36)	71.4 (58.06-81.87)	61.8 (48.52-73.46)	43.9 (33.55-54.82)	71.4 (55.49-83.37)
Accuracy	75.3 (64.75-84.01)	77.7 (67.31-85.97)	69.4 (58.47-78.95)	54.1 (42.96-64.98)	74.1 (63.48-83.02)

ADCr, apparent diffusion coefficient ratio; AUC, area under curve; ERc, corticomedullary phase enhancement ratio; ERd, delayed phase enhancement ratio; ERn, nephrogenic phase enhancement ratio; NPV, negative predictive value; PPV, positive predictive value; RCC, renal cell carcinoma; T2SIR, T2 signal intensity ratio.
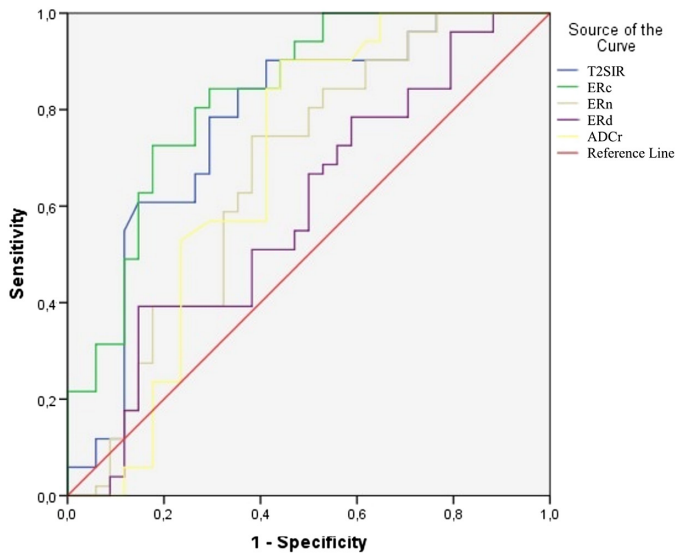
researchers have aimed to differentiate renal tumor subtypes based on the degree of enhancement of tumors on contrast enhanced computerized tomography and MRIs.[20-23] These researchers identified statistically significant differences between the degree of enhancement in different RCC subtypes. Also, this made it difficult to distinguish clear cell RCC with contrast-enhancement alone, as the contrast levels of clear cell RCC and other renal cortical tumors, especially oncocytoma and angiomyolipoma, were generally similar.[24] In our work, there was a statistically significant difference between papillary RCC and both clear cell RCC and oncocytoma in ERc and ERn ($P < .008$). There was a statistically significant difference between chromophobe RCCs and clear cell RCCs in ERc and between chromophobe RCCs and oncocytoma in ERn and ERd ($P = .031$, $P = .038$ and $P = .031$, respectively). In the logistic regression analysis between clear cell RCC and other renal cortical tumors, the parameters that were statistically significant in both univariate and multivariate analyses were ERc and ERn ($P < .001$). The most effective parameter in the differentiation of the 2 groups was ERc, with a cutoff value of 283.6; sensitivity was 80.4%, specificity was 73.5%, positive predictive value was 82%, negative predictive value was 71.4%, and accuracy was 77.7%. Multiparametric magnetic resonance imaging can be used to distinguish clear cell RCC from other renal cortical tumors in patients with small tumors that are less likely to be diagnosed by biopsy or who are at high medical risk for interventional procedures.

Our study has some limitations. First, it is designed retrospectively. While readers are blinded to the final pathology, there is inherent bias in this structure. Second, ROI locations and assessments were made in agreement with 2 radiologists, and interobserver variability was not calculated. Studies with more than 1 reader will confirm these results. Third, the number of chromophobe RCCs in our study was low in proportion to the incidence of this subtype among society. At last, our study did not cover the entire RCC spectrum, as undifferentiated RCC subtypes and other rarer subtypes were not included in our study. However, we do not think these 3 subtypes we selected affect the power of our study as they constitute 90% of all RCCs encountered in clinical practices.

CONCLUSION

We think that the diagnostic sensitivity and specificity of mpMRI, including T2SIR and ERc, which is used to distinguish clear cell RCC from other common subtypes of renal cortical tumors, is high. The use of the quantitative parameters of mpMRI may be useful in treatment planning in elderly patients with comorbidities at high risk for biopsy or surgery, or to encourage active surveillance where appropriate.

Figure 6. Receiver operating characteristic curves for parameters T2 signal intensity ratio (T2SIR), corticomedullary phase enhancement ratio (ERc), nephrogenic phase enhancement ratio (ERn), delayed phase enhancement ratio (ERd), and apparent diffusion coefficient ratio (ADCr).

and a hypointense stellate scar may be found in the central part.[14] In a study, Cornelis et al[15] determined that the T2 signal ratio was the lowest in papillary RCCs and AMLs of renal cortical tumors, while this rate was higher in chromophobe RCCs, clear cell RCCs, and oncocytomas. In our work, parallel to the literature, T2SIR was the lowest in papillary RCCs, and there was a statistically significant difference in the differentiation from other types of tumors. In the univariate analysis, T2SIR was statistically different in distinguishing between clear cell RCCs and other renal cortical tumors ($P = .004$). Between the 2 tumor groups, sensitivity was 78.4% and specificity was 70.6% in T2SIR with a cutoff value of 107.2. The use of TSIR in multiparametric MRI plays a crucial role in the differentiation of subtypes of renal cortical tumors by increasing the diagnostic efficiency.

Diffusion-weighted imaging, which provides information on the cell density, has been valuable in oncological imaging and has also been used for differentiation of RCC subtypes. Most researchers briefed that the ADC values of clear cell RCCs are higher compared to RCC subtypes but are similar to oncocytomas.[16,17] As ADC values vary based on devices and magnetic field strength, we used the ADCr in our study, which we considered could eliminate these differences. There are few studies in the literature that differentiate RCCs using the ADCr.[15,18,19] Zhong et al[18] used ADCr to distinguish oncocytoma from chromophobe RCCs and found a statistically significant difference. In our study, the highest ADCr was in oncocytoma and the lowest ADCr was in papillary RCCs. There was a statistically significant difference between papillary RCCs and oncocytoma and between papillary RCC and clear cell RCC ($P < .001$). The findings of our study were parallel to those of the study by Cornelius et al.[15] In differentiating clear cell RCC and other renal cortical tumors, the sensitivity was 84.3 and the specificity was 58.8, with a cutoff value of 0.80 in ADCr. We think that this may be employed as a determining parameter in the differentiation of RCC subtypes, regardless of the device.

As clear cell RCC is known to have higher vascularity than other RCC subtypes, such as chromophobe RCCs and especially papillary RCCs,

REFERENCES

1. Muglia VF, Prando A. Renal cell carcinoma: histological classification and correlation with imaging findings. *Radiol Bras*. 2015;48(3):166-174. [CrossRef]
2. Manley BJ, Hsieh JJ. Sarcomatoid renal cell carcinoma: genomic insights from sequencing of matched sarcomatous and carcinomatous components. *Transl Cancer Res*. 2016;5(suppl 2):S160-S165. [CrossRef]
3. Deng J, Li L, Xia H, et al. A comparison of the prognosis of papillary and clear cell renal cell carcinoma: evidence from a meta-analysis. *Med (Baltim)*. 2019;98(27):e16309. [CrossRef]
4. Wobker SE, Williamson SR. Modern pathologic diagnosis of renal oncocytoma. *J Kidney Cancer VHL*. 2017;4(4):1-12. [CrossRef]
5. Sanchez A, Feldman AS, Hakimi AA. Current management of small renal masses, including patient selection, Renal Tumor Biopsy, Active Surveillance, and Thermal Ablation. *J Clin Oncol*. 2018;36(36):3591-3600. [CrossRef]
6. Leone AR, Diorio GJ, Spiess PE, Gilbert SM. Contemporary issues surrounding small renal masses: evaluation, diagnostic biopsy, nephron sparing, and novel treatment modalities. *Oncology (Williston Park)*. 2016;30(6):507-514.
7. Pagnini F, Cervi E, Maestroni U, et al. Imaging guided percutaneous renal biopsy: do it or not? *Acta Biomed*. 2020;91(8-S):81-88. [CrossRef]
8. Brachemi S, Bollée G. Renal biopsy practice: what is the gold standard? *World J Nephrol*. 2014;3(4):287-294. [CrossRef]
9. Hogan JJ, Mocanu M, Berns JS. The native kidney biopsy: update and evidence for best practice. *Clin J Am Soc Nephrol*. 2016;11(2):354-362. [CrossRef]
10. Hötker AM, Mazaheri Y, Wibmer A, et al. Differentiation of clear cell renal cell carcinoma from other renal cortical tumors by use of a quantitative multiparametric MRI approach. *AJR Am J Roentgenol*. 2017;208(3):W85-W91. [CrossRef]
11. Diaz de Leon A, Costa D, Pedrosa I. Role of multiparametric MR imaging in malignancies of the urogenital tract. *Magn Reson Imaging Clin N Am*. 2016;24(1):187-204. [CrossRef]
12. Lu D, Yuan W, Zhu Q, Ye J, Zhu W, Chen W. Comparative study of CT and MRI appearances in mucinous tubular and spindle cell carcinoma and papillary renal cell carcinoma. *Br J Radiol*. 2021;94(1126):20210548. [CrossRef]
13. Wang ZJ, Zagoria RJ. Invited commentary on "differentiation of solid renal tumors with multiparametric MR imaging". *RadioGraphics*. 2017;37(7):2042-2044. [CrossRef]
14. Lopes Vendrami C, Parada Villavicencio C, Dejulio TJ, et al. Differentiation of solid renal tumors with multiparametric MR imaging. *RadioGraphics*. 2017;37(7):2026-2042. [CrossRef]
15. Cornelis F, Tricaud E, Lasserre AS, et al. Routinely performed multiparametric magnetic resonance imaging helps to differentiate common subtypes of renal tumours. *Eur Radiol*. 2014;24(5):1068-1080. [CrossRef]
16. Wang H, Cheng L, Zhang X, et al. Renal cell carcinoma: diffusion-weighted MR imaging for subtype differentiation at 3.0 T. *Radiology*. 2010;257(1):135-143. [CrossRef]
17. Cova M, Squillaci E, Stacul F, et al. Diffusion-weighted MRI in the evaluation of renal lesions: preliminary results. *Br J Radiol*. 2004;77(922):851-857. [CrossRef]
18. Zhong Y, Wang H, Shen Y, et al. Diffusion-weighted imaging versus contrast-enhanced MR imaging for the differentiation of renal oncocytomas and chromophobe renal cell carcinomas. *Eur Radiol*. 2017; 27(12):4913-4922. [CrossRef]
19. Ludwig DR, Ballard DH, Shetty AS, Siegel CL, Yano M. Apparent diffusion coefficient distinguishes malignancy in T1-hyperintense small renal masses. *AJR Am J Roentgenol*. 2020;214(1):114-121. [CrossRef]
20. Young JR, Margolis D, Sauk S, Pantuck AJ, Sayre J, Raman SS. Clear cell renal cell carcinoma: discrimination from other renal cell carcinoma subtypes and oncocytoma at multiphasic multidetector CT. *Radiology*. 2013;267(2):444-453. [CrossRef]
21. Vargas HA, Chaim J, Lefkowitz RA, et al. Renal cortical tumors: use of multiphasic contrast-enhanced MR imaging to differentiate benign and malignant histologic subtypes. *Radiology*. 2012;264(3):779-788. [CrossRef]
22. Kim JH, Bae JH, Lee KW, Kim ME, Park SJ, Park JY. Predicting the histology of small renal masses using preoperative dynamic contrast-enhanced magnetic resonance imaging. *Urology*. 2012;80(4):872-876. [CrossRef]
23. Sun MR, Ngo L, Genega EM, et al. Renal cell carcinoma: dynamic contrast-enhanced MR imaging for differentiation of tumor subtypes--correlation with pathologic findings. *Radiology*. 2009;250(3):793-802. [CrossRef]
24. Pierorazio PM, Hyams ES, Tsai S, et al. Multiphasic enhancement patterns of small renal masses (≤4 cm) on preoperative computed tomography: utility for distinguishing subtypes of renal cell carcinoma, angiomyolipoma, and oncocytoma. *Urology*. 2013;81(6):1265-1271. [CrossRef]

Cutis Verticis Gyrata: A Rare Finding in Cranial Magnetic Resonance Imaging that Is Usually Overlooked
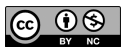
Derya Güçlü[ID], Osman Şinasi Oğuz[ID], Hayri Oğul[ID]

Department of Radiology, Düzce University, Faculty of Medicine, Düzce, Turkey

Abstract

Objective: Cutis verticis gyrata is a rare condition of scalp thickening, characterized by deep grooves and gyriform ridges that can be observed on computed tomography scans and magnetic resonance imaging. It is a benign and asymptomatic condition, but sometimes, it may be associated with some systemic diseases in the secondary form.

Methods: Review of the 4026 magnetic resonance imaging studies from a clinics' archive revealed 29 patients with cutis verticis gyrata. Obtained images were re-evaluated for symmetry, localization, and direction. History and previous medical records of the subjects were evaluated, and laboratory or clinic findings that could be related to cutis verticis gyrata were noted.

Results: Around 44.8% (n = 13) of the subjects were male and 55.2% (n = 16) were female. Age range was 28-87 years with a mean of 61.10 ± 15.25 years. Evaluation of the history and previous medical records of the subjects revealed no laboratory and no clinic findings that could be related with cutis verticis gyrata; therefore, the cases were accepted as primary. About 21 patients had bilateral involvement, which was asymmetric in 8 of them; 24 patients (82.8%) had a chronic disease, 11 out of them (37.9%) had diabetes mellitus, 15 (51.7%) had hypertension; 18 cases (62.1%) had magnetic resonance imaging signs of small vessel disease.

Conclusion: When encountered during radiological imaging, clinicians must be aware of possible diseases that may be associated with cutis verticis gyrate, and further investigations may be performed to rule out these diseases.

Keywords: Cutis verticis gyrata, magnetic resonance imaging

INTRODUCTION

Cutis verticis gyrata (CVG) is a rare condition of scalp thickening, characterized with deep grooves and gyriform ridges, sometimes giving a spiky cogwheel appearance on computerized tomography (CT) scans and magnetic resonance imaging (MRI).[1,2] Cutis verticis gyrata has a primary form, where there is no known etiology, and this form may be associated with mental retardation, cerebral palsy, epilepsy, cataract, and blindness.[3,4] It may also be secondary to local scalp diseases, genetic syndromes, minoxidil and testosterone use, and endocrine and systemic diseases like acromegaly.[3] It is estimated that CVG is seen in 1 in 100 000 males and in 0.026 in 100 000 females.[4] In histopathological examination, there is hypertrophy of sebaceous structures with no evidence of collagen thickening. Overgrowth of the scalp in the form of CVG is observed in 10%-15% of acromegaly patients. The ridges of the skin in CVG develop due to the overgrowth of the scalp on a narrow surface limited by scalp fascia. Secondary form of CVG regresses after the treatment of the underlying condition, but sometimes, surgical interventions may be necessary.[4]

In the present article, we aimed to document 29 cases who had CVG apparent on MRI images. We obtained demographic and clinical data of the cases, like the presence of systemic diseases, and aimed to discuss available information and compare this with that of similar reports from the literature.

METHODS

Patients and Magnetic Resonance Imaging Protocol

Our MRI archive containing 4026 MRI studies of the head for the period from October 2021 to October 2022 was reviewed after obtaining local ethical committee's approval. Review of the MRI archive revealed 29 patients with CVG. A 3T MRI (MAGNETOM Skyra, Siemens Healthcare, Erlangen, Germany) had been used. The performed magnetic resonance examinations yielded 3-mm thick coronal and axial images. Patients were examined with conventional sequences like sagittal spin-echo T1-weighted images (T1WI), axial and coronal spin-echo T2-weighted images (T2WI), and axial fluid attenuation inversion recovery sequence (FLAIR) and standard head coils were used. Obtained images were re-evaluated for symmetry, localization, and direction. History and previous medical records of the subjects were evaluated, and laboratory or clinic findings that could be related to CVG were noted.
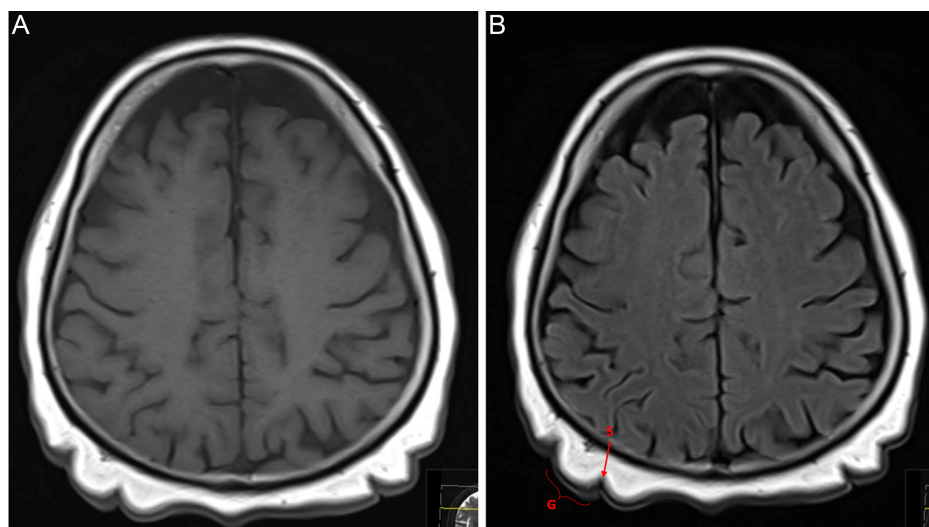
Figure 1. T1- and T2-weighted axial magnetic resonance images demonstrate cutis verticis gyrata on the scalp without any cerebral abnormalities. G, gyriform structure; S, sulcal morphology.

Statistical Analysis

Statistical analyses were made with the International Business Machines' Statistical Package for the Social Sciences version 22.0. (IBM SPSS Corp.; Armonk, NY, USA). The distribution of the numerical data was analyzed with Shapiro–Wilk test; Independent samples *t*-test was used for group comparisons. Analyses of categorical variables were made with Fisher's exact or Fisher–Freeman–Halton test. Descriptive statistics for numerical variables were given as mean and standard deviations and for categorical variables with numbers and percentages. A statistically significant value of *P*< .05 was used.

RESULTS

Around 44.8% (n=13) of the subjects were male and 55.2% (n=16) were female. Age range was 28-87 years with a mean of 61.10 ± 15.25 years. None of the patients had a complaint related to scalp thickening and CVG was observed incidentally during brain MRIs, performed for various other indications. Evaluation of the history and previous medical records of the subjects revealed no laboratory and no clinic findings that could be related to CVG; therefore, the cases were accepted as primary.

Characteristic ridges and grooves of the scalp were apparent on coronal images and they were mostly seen at the vertex (Figure 1). They were running anteroposteriorly and extended up to the occipital region. Signal intensities of the ridges and grooves were normal. No endocrine investigation was found in their records. All CVG cases had a generalized thickening of the skin, but in only 5 cases, the scalp was extensively corrugated and had a wavy appearance, demonstrating a cogwheel pattern.

MAIN POINTS

- Cutis verticis gyrata (CVG) is a rare condition of scalp thickening.
- Cutis verticis gyrata is characterized by deep grooves and gyriform ridges, sometimes giving a spiky cogwheel appearance on thickening scalp on sectional imaging.
- This condition has a primary and a secondary form.
- The secondary form of the disease can be associated with many systemic conditions.

About 21 patients had bilateral involvement, which was asymmetric in 8 of them (Figure 2). In all patients, CVG was seen in the vertex with variable anterior or posterior extensions to the frontal or occipital regions. Transverse folds were better visualized on the sagittal plane, whereas longitudinal CVG folds were clearer on the coronal plane. Calvarium was normal in all patients.

Co-existing diseases are listed in Table 1. Totally 24 patients (82.8%) had a chronic disease and 11 of them (37.9%) had diabetes mellitus (DM) and 15 (51.7%) had hypertension (HT). In 18 cases (62.1%), there were MRI signs of small vessel disease (SVD) (Figure 3). One patient also had normal pressure hydrocephalus (Figure 4).

DISCUSSION

Cutis verticis gyrata has a primary and a secondary form. The cases in the present study had no condition in their medical records that would be related to CVG; therefore, all cases were considered primary. Although these were all primary cases, there was no mental retardation, cerebral palsy, epilepsy, cataract, and blindness either, which are the conditions that could be associated with the primary form. This form of primary CVG, which is not associated with these abnormalities, is called the primary essential form.[4]

Primary essential form constitutes 79.6% of all primary cases,[5] whereas all cases of our study group were of the primary essential type. In a larger group of CVG patients, non-essential type would also be encountered and the ratio that we found may change.

Asymptomatic cases of essential primary CVG, where the ridges and grooves are not that prominent, may be overlooked by both the clinicians and radiologists.[5] There were only 5 cases in our group who had prominent grooves and ridges. It is quite possible to overlook milder cases, especially when the orientation of the ridges and grooves is parallel to the imaging plane.

The characteristics of the ridges and grooves were similar to other studies. It was reported that the ridges and grooves have usually an antero-posterior direction except for the ones in the occipital region, where
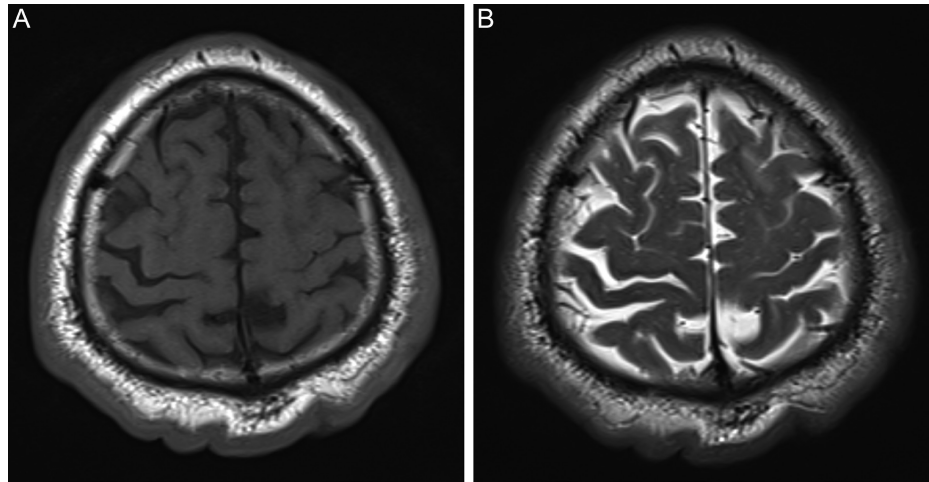
Figure 2. Axial T1- and T2-weighted magnetic resonance images show mild and asymmetric cutis verticis gyrata morphologies.

Table 1. Co-existing Conditions of CVG

	n	%
Chronic disease	24	100
Diabetes mellitus (DM)	5	20.8
Hypertension (HT)	9	37.5
DM+HT	6	25
Other diseases	4	16.7

CVG, cutis verticis gyrate.

they are usually obliquely oriented.[5] A similar orientation pattern was observed also in our cases.

Cutis verticis gyrata is seen in 1 in 100 000 males and in 0.026 in 100 000 females.[4] Around 29 CVG patients on 4026 MRI images appear to be a very high rate. An explanation might be that the CVG prevalence given in the present article is not from a radiological study. Although there are no big series reported yet in the literature, we believe that CVG prevalence, especially the prevalence of the secondary form, might increase with the increase in the use of cross-sectional imaging.

In addition, there are studies that report incidences of up to 12.5% in certain psychiatric diseases.[6,7]

Male to female ratio in the present study was 13 : 16. Cutis verticis gyrata was more common in female patients, which is in contrast with Okamoto et al's[5] study where it was reported that male to female ratio was 5-6 : 1. The cases from the present study consist of non-symptomatic CVG cases who had undergone MRI for different indications. The cases we detected may not be representing all CVG cases during the same time period and our findings may not be reflecting a correct male-to-female ratio.

Both HT and DM seemed frequent in the CVG cases. The prevalence of DM in Turkey is 16.5% according to the TURDEP II study from 2013,[8] whereas the prevalence of HT is 30.3% according to Sengul et al[9] Our CVG group has a relatively higher age (61.10 ± 15.25 years) in contrast to the study populations of the prevalence studies, which consist of adults older than 20 years of age. It is known that HT and DM are more frequent in older ages.[8,9] The increased rate of HT and DM among CVG cases could not be associated with the presence of
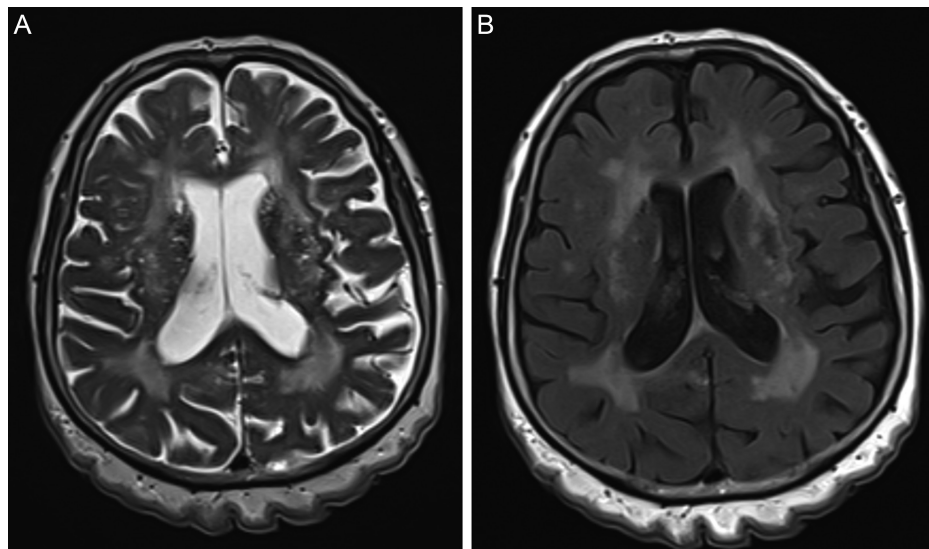

Figure 3. Axial T1- and T2-weighted magnetic resonance images show small vessel plaques associated with cutis verticis gyrata.
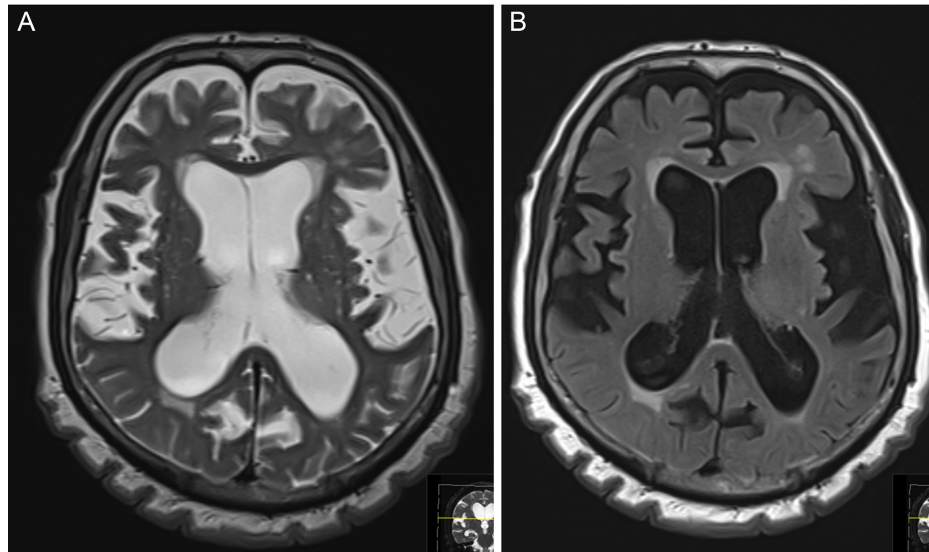
Figure 4. Axial T1- and T2-weighted magnetic resonance images reveal coexistence of both cutis verticis gyrata and normal pressure hydrocephalus.

CVG, because we do not have a comparable prevalence data from a matching non-CVG population.

In 62.1% of cases, there were MRI signs of SVD. White matter lesions and lacunar infarcts are referred to as SVD and it is a common finding in MRI and CT images of elderly people. Small vessel disease is related to some diseases that are vascular risk factors like atherosclerosis, hypertension, DM, and atrial fibrillation.[10,11] We observed higher percentages of both hypertension and DM in our cases; therefore, the percentage of SVD was also relatively high as expected. Chronic kidney disease, obstructive sleep apnea, current and former smoking, and branch atheromatous disease are other risk factors for SVD.[12]

The present study was conducted retrospectively. That the evaluation was made on routine head and neck cranial imaging, rather than specific imaging planned especially for CVG, has been a limitation of the present study. A prospective study with detailed maxillofacial examination data and sequence optimization for a better scalp evaluation could reveal more reliable data. According to our knowledge, there are no established criteria for the radiological distinction of CVG from cutis laxa (CL). Cutis verticis gyrata is basically a dermatological diagnosis. For the distinction of CVG from CL, some physical examination maneuvers are necessary on a clinical basis. The retrospective setting of the present study was not appropriate to make a clear distinction because each patient had not been examined specifically for CVG. Therefore, it is possible that some of our cases might have CL. This has been another major limitation of our study. Further studies are necessary, in which clinicians and radiologists will work in cooperation.

In conclusion, CVG is a rare and benign condition of the scalp characterized by deep grooves, gyriform ridges, and thickened skin. There is a primary and secondary form. The secondary form is associated with systemic diseases like acromegaly. Neuroradiologists should be aware of this scalp condition to interpret its characteristic radiological findings correctly and remind clinicians to rule out possible systemic diseases that may be underlying or co-existing with this benign condition.

REFERENCES
1. Kolawole TM, Al Orainy IA, Patel PJ, Fathuddin S. Cutis verticis gyrata: its computed tomographic demonstration in acromegaly. *Eur J Radiol*. 1998;27(2):145-148. **[CrossRef]**
2. Alorainy IA. Magnetic resonance imaging of cutis verticis gyrata. *J Comput Assist Tomogr*. 2008;32(1):119-123. **[CrossRef]**
3. Landenberger GMC, Ongaratti BR, Pereira-Lima JFS, Oliveira MDC. Cutis verticis gyrata: a cutaneous finding in acromegaly. *An Bras Dermatol*. 2022;97(3):369-371. **[CrossRef]**
4. Walia R, Bhansali A. Cutis verticis gyrata. *BMJ Case Rep*. 2011. **[CrossRef]**
5. Okamoto K, Ito J, Tokiguchi S, Ishikawa K, Furusawa T, Sakai K. MRI in essential primary cutis verticis gyrata. *Neuroradiology*. 2001;43(10): 841-844. **[CrossRef]**
6. Snyder MC, Johnson PJ, Hollins RR. Congenital primary cutis verticis gyrata. *Plast Reconstr Surg*. 2002;110(3):818-821. **[CrossRef]**
7. Chang GY. Cutis verticis gyrata, underrecognized neurocutaneous syndrome. *Neurology*. 1996;47(2):573-575. **[CrossRef]**
8. Satman I, Omer B, Tutuncu Y, et al. Twelve-year trends in the prevalence and risk factors of diabetes and prediabetes in Turkish adults. *Eur J Epidemiol*. 2013;28(2):169-180. **[CrossRef]**
9. Sengul S, Akpolat T, Erdem Y, et al. Changes in hypertension prevalence, awareness, treatment, and control rates in Turkey from 2003 to 2012. *J Hypertens*. 2016;34(6):1208-1217. **[CrossRef]**
10. van Norden AG, de Laat KF, Gons RA, et al. Causes and consequences of cerebral small vessel disease. The RUN DMC study: a prospective cohort study. Study rationale and protocol. *BMC Neurol*. 2011;28:11-29.
11. Chojdak-Łukasiewicz J, Dziadkowiak E, Zimny A, Paradowski B. Cerebral small vessel disease: a review. *Adv Clin Exp Med*. 2021;30(3):349-356. **[CrossRef]**
12. Gez S, İnce B, Tütüncü M, et al. Prevalence of clinical manifestations and neuroimaging features in cerebral small vessel disease. *Clin Neurol Neurosurg*. 2022;217:107244. **[CrossRef]**

The Role of 3 Tesla Diffusion Weighted-Magnetic Resonance Imaging and Apparent Diffusion Coefficient Mapping with Aging and Gendering in Primary Parotid Tumors: Preoperative Foresight of Histopathological Subtypes

Abdurrahim Dusak[1], Adem Ağyar[1], Mustafa Çelik[2], Saime Shermatova[1], Veysel Kaya[1], Muhammed Emin Güldür[1]

[1]Department of Radiology, Harran University, Faculty of Medicine, Şanlıurfa, Turkey
[2]Department of Ear Nose & Throat, Harran University, Faculty of Medicine, Şanlıurfa, Turkey

Abstract

Objective: Preoperative foresight of primary parotid tumors is decisive for surgical planning. We aimed to assign the role of 3 tesla diffusion-weighted magnetic resonance (3T DW-MR) imaging, apparent diffusion coefficient (ADC) mapping, aging, and gendering in differentiating the primary parotid tumor subtypes on the basis of histopathological correlation.

Methods: Thirty-one primary parotid tumors and tumor-free contralateral parotid glands of the same patients were evaluated retrospectively. The 3T DW-MR imaging, ADC, calculated apparent diffusion coefficient value, and demographic data were compared, and receiver operating characteristic analysis was carried out with histopathological results. A *P*-value <.05 was considered to be statistically significant.

Results: The apparent diffusion coefficient value of primer parotid tumors (n=31) was $1.43 \pm 0.51 \times 10^{-3}$ mm^2/s, of benign parotid tumors (n=25) was $1.61 \pm 0.38 \times 10^{-3}$ mm^2/s [Warthin tumors (n=7): $1.14 \pm 0.20 \times 10^{-3}$ mm^2/s, pleomorphic adenomas (n=18): $1.80 \pm 0.24 \times 10^{-3}$ mm^2/s], of malignant parotid tumors (n=6) was $0.69 \pm 0.25 \times 10^{-3}$ mm^2/s, and of normal parotid gland (n=31) was $0.94 \pm 0.18 \times 10^{-3}$ mm^2/s. Statistically, an intergroup differences was found between malignant and benign parotid tumors ($P < .001$). An intragroup difference was found between Warthin tumor and pleomorphic adenoma ($P < .001$). The results showed that aging and gendering were significantly different within primary parotid tumors ($P < .001$).

Conclusion: Using the results of 3T DW-MR imaging and ADC mapping with aging and gendering may provide preoperative primary parotid tumor characterization. The ADC value and age and gender might be useful in differentiating benign malign primary parotid tumors including subtypes such as Warthin tumor and pleomorphic adenoma. This aspect might be applied in routine applications.

Keywords: 3T DW-MR imaging, ADC mapping, primary parotid tumor, benign parotid tumor, Warthin tumor, pleomorphic adenoma, malignant parotid tumor

INTRODUCTION

The largest salivary glands and parotid gland have a specific structure; saliva is secreted through the parotid duct and digestion starts in the mouth.[1,2] Reports observed that parotid glands have a large variety of textures with aging and gendering and have a different histopathological subgroup of primary parotid tumors.[3-6] Pleomorphic adenomas display myxoid and chondroid matrices.[7] Adenoid carcinoma has myxoid, hyalinized, and mucinous matrices.[8] The management of parotid tumors needs a detailed figure of the histopathological processes affecting the parotid glands. While local residue and recurrence risk are high in pleomorphic adenomas (>80%), they are less in Warthin tumors (<5%) with regard to the same surgical procedure.[9,10] Determining a convenient surgical procedure for primary parotid tumors is not only a differential diagnosis between groups of malignant or benign parotid tumors but also a distinction of benign histopathological subgroups including Warthin tumor and pleomorphic adenoma.[8,11]

Image-guided fine-needle aspiration biopsy (IG-FNAB) is approved as a useful method for preoperative differential diagnosis, with cytopathological accuracy between 80% and 90% in primary parotid tumors.[10,12] IG-FNAB risk might be a potential inoculation, which can spearhead a higher possibility of local residue recurrence, particularly in malignant parotid tumors and pleomorphic adenomas.[8,11] The cytopathological differential diagnosis for several primary parotid tumors might be unfeasible or difficult.[9,10] Pleomorphic adenomas have a labile histopathological design

that could mimic adenoid and mucoepidermoid carcinomas.[13] By using IG-FNAB alone, the distinction between adenoma and adenocarcinoma is mostly impossible.[10]

Magnetic resonance (MR) imaging can identify the characteristics of primary parotid tumors and determine the contiguity and extension.[14,15] However, routine MR imaging cannot differentiate primary parotid tumors from histopathological subtypes by preoperative planning and operation procedure alone.[10-13] Diffusion-Weighted (DW) MR imaging, apparent diffusion coefficient (ADC) mapping, and calculated ADC values depict random molecular diffusion of the parotid gland and affect gland perfusion and salivating.[15-17] The adjustment b-factor is critical and decisive in determining ADC mapping. There is an inverse relationship between the ADC value and the b-factor. High b-factors are preferred to minimize the effect of the parotid gland.[18]

The parotid gland has a unique texture that increases fat accumulation and other chances of aging and gendering.[19,20] Primary parotid tumors contain complex tissues composed of myxomatous and lymphoid matrices and cystic and necrotic tissues.[3] Primary parotid tumors may not be homogeneous due to the presence of cystic areas, necrosis, degeneration, or bleeding.[9] Therefore, the evaluation of a large region of interest (ROI) in the myxomatous tumor might have misleading results in the primary parotid tumors.[21,22] DW MR imaging and ADC mapping can reveal biophysical disturbances associated with histopathological alterations in the tumoral process and might segregate with gantry strength.[23,24] To minimize this dilemma and achieve optimum image quality and tissue, characterization using 3 tesla (3T) DW-MR imaging with a 64-channel head and neck coil appears necessary.[3,18] Demographic data might be useful in distinguishing primary parotid tumors.[25] Benign parotid tumors are seen in younger patients, whereas Warthin tumor tendency is seen in elderly patients.[26] Gender was not dominant in the primary parotid tumors, while male predominance was shown in Warthin tumor.[5] In the current study, we investigated 3T DW-MR imaging and ADC mapping using aging and gendering of the benign and malign primary parotid tumor

---

MAIN POINTS

- The largest salivary glands and parotid gland have a specific structure. Parotid glands have a large variety of textures with aging and gendering and have a different histopathological subgroup of primary parotid tumors.

- Management of parotid tumors needs a detailed figure of the histopathological processes affecting the parotid glands. While local residue and recurrence risk are high in pleomorphic adenomas (>80%), they are less in Warthin tumors (<5%) with regard to the same surgical procedure.

- The apparent diffusion coefficient (ADC) value of pleomorphic adenoma was significantly higher than that of Warthin tumor and malignant parotid tumor. The ADC value of Warthin tumor was lower than that of the pleomorphic adenoma and higher than that of the malignant parotid tumor. By aging in pleomorphic adenoma was lower when compared to Warthin tumor and malign parotid tumor, and gendering in Warthin tumor was male dominance when compared to pleomorphic adenoma and malign parotid tumor. 3 Tesla DW-MR imaging and ADC mapping with aging and gendering might be useful in differential diagnosing of malignant and benign parotid tumors including Warthin tumors and pleomorphic adenomas.

---

and common subtypes of benign parotid tumors such as Warthin tumor and pleomorphic adenoma with histopathological correlation and to check our data with previous literary instructions.

METHODS

The institutional ethics committee approved our study (date: July 5, 2018, Session: 07, Decision: 18.07.24). Our medical study had retrospective consideration and was administered following the Helsinki Declaration. Moreover, this research was approved by the corporate ethics board. Thirty-one patients (20 females, 11 males; mean age 43 (18-81) years) who had primary parotid tumors were included. The study group consisted of patients with operated primary parotid tumors. The control group was established as contralateral normal parotid glands of the same patients. The exclusion criteria were poor MR imaging, simple cyst, and metastatic parotid tumors. The 3T-DW MR imaging of patients was performed between 2016 and 2018. The study was conducted at Şanlıurfa Harran University Hospital Radiology Department.

Magnetic Resonance Imaging Protocol

Each patient with a primary parotid tumor underwent MR imaging using the 3T MR scanner system (Magnetom Skyra, Siemens Healthcare, Erlangen, Germany) and using a 64-channel phasedarray head and neck coil. Routine MR imaging was performed with T1-weighted (T1W) (Time to Repetition (TR): 300 ms, Time to Echo (TE): 2 ms, Flip Angle (FA): 70°), T2W (TR: 4930 ms, TE: 91 ms, FA: 180°), turbo spin echo (tse), and fat saturation (fs) T1W (TR: 822 ms, TE: 13 ms, FA: 160°) images in the axial and T2W (TR: 4150 ms, TE: 37 ms, FA: 160°) tse images in the coronal plane. After an intravenous injection rate of 3 mL/s of 0.1 mmol/kg Gadobutrol (Gadovist; Bayer Schering Pharma, Berlin, Germany) fs T1W (TR: 822 ms, TE: 13 ms, FA: 160°) axial and T1W (TR: 300 ms, TE: 2 ms, FA: 700) sagittal and coronal images were obtained. 3 Tesla DW MR imaging (TR: 6400 ms, TE: 98 ms, FA: 90°, number of excitations (nex: 1, interslice: 0.5 mm, field: 22 × 22, thickness: 5 mm, matrix: 128 × 128) was obtained in an axial plane using an echo-planar Spin Echo (SE) sequence with a b value of 1000 mm^2/s tracing on conventional MR imaging. The acquisition time for 3T DW-MR images was 46 s.

Magnetic Resonance Imaging Processing and Data Analysis

Apparent diffusion coefficient mapping was generated from 3T DW-MR images for each patient, and ADC values were calculated manually by using the ellipsoid ROI for the appropriate placement of the primary parotid tumor and the contralateral normal parotid gland, in the same patient with routine MR image guiding, excluding cystic and necrotic areas. The ADC value from the contralateral normal gland was calculated in the same patient from the control group. For each measurement of parotid tumor and normal parotid glands, the ROI was placed at 4 mm^2 as symmetrically as possible except for intra-parotid lymph nodes and retromandibular vein.

Histopathological Analysis

After 3T DW-MR imaging, histopathological examinations were handled for the primary parotid tumors that were surgically resected to support definitive histopathological data in all patients. An experienced pathologist (M.E.G.) evaluated all surgical resection specimens. Histopathological subtypes of the primary parotid tumors (n=31) were benign parotid tumors (n=25), including Warthin tumor (n=7), pleomorphic adenoma (n=18), and malignant parotid tumor (n=6), including mucoepidermoid carcinoma (n=2), squamous cell carcinoma (n=2), non-Hodgkin lymphoma (n=1), and leiomyosarcoma (n=1).

Statistical Analysis

The obtained ADC values of the primary parotid tumor and contralateral normal parotid gland from all patients were evaluated by the Shapiro–Wilk normality test to see whether ADC values showed normal distribution. One-way analysis of variance (ANOVA) and post-hoc least significant difference test (Tukey) were used for normal distributed data. The data were recorded as mean ADC value ± SD. Whether the data were normally distributed or not was evaluated with the Shapiro–Wilk test. For comparisons between the 2 groups, normally distributed parameters were evaluated with the Student's t-test and non-normally distributed parameters were evaluated with Mann–Whitney U test. For comparisons between more than 2 groups, normally distributed parameters were evaluated with 1-way ANOVA and non-normally distributed parameters were evaluated with Kruskal–Wallis H test. Results were expressed as the mean difference and P-value. Differences among the ADC values and demographic data for malign and benign parotid tumors, within common benign parotid tumors including Warthin tumor and pleomorphic adenoma, and normal parotid gland were evaluated using 1-way ANOVA. If the P-value was significant, a multiple comparison test was used to determine the differences between groups. We averaged the ADC value of primary parotid tumors and healthy parotid glands of each patient. Statistical analyses were performed with Statistical Package for the Social Sciences version 23.0. (IBM SPSS Corp.; Armonk, NY, USA) . 3 Tesla DW MR image analysis was implemented independently by 2 head and neck radiologists (A.D. and V.K.). The difference between malignant and benign primary parotid tumors and common benign subtypes of Warthin tumor and pleomorphic adenoma was investigated, and the threshold value was determined using receiver operating characteristic (ROC) analysis. Statistically significant value was accepted as $P < .05$.

RESULTS

Thirty-one primary parotid tumors [7 Warthin tumors, 18 pleomorphic adenomas, 6 malignant parotid tumors (2 mucoepidermoid carcinomas, 2 squamous cell carcinoma, 1 non-Hodgkin's lymphoma, and 1 leiomyosarcoma)] and 31 contralateral normal parotid gland were included in the current study.

The calculated ADC values (Table 1) for histopathologically confirmed primary parotid tumors were demonstrated as follows; the primary parotid tumor: $1.43 \pm 0.51 \times 10^{-3}$ mm^2/s, the benign parotid tumor: $1.61 \pm 0.38 \times 10^{-3}$ mm^2/s [Warthin tumor: $1.14 \pm 0.20 \times 10^{-3}$ mm^2/s (Figure 1) and pleomorphic adenoma: $1.80 \pm 0.24 \times 10^{-3}$ mm^2/s (Figure 2)], the

Table 1. ADC Mapping of Primary Parotid Tumors

Groups	n	Gender	Age (Years)	ADC Value (Mean ± SD)
Primer parotid tumor	31	20 male/11 female	42.9 ± 16.1 (18-81)	$1.43 \pm 0.51 \times 10^{-3}$ mm^2/s
Benign parotid tumor	25	16 male/9 female	39.2 ± 14.5 (18-76)	$1.61 \pm 0.38 \times 10^{-3}$ mm^2/s
Warthin tumor	7	7 male/0 female	55.0 ± 12.8 (39-76)	$1.14 \pm 0.20 \times 10^{-3}$ mm^2/s
Pleomorphic adenoma	18	10 male/8 female	33.1 ± 09.8 (18-50)	$1.80 \pm 0.24 \times 10^{-3}$ mm^2/s
Malign parotid tumor	6	4 male/2 female	58.3 ± 13.7 (42-81)	$0.69 \pm 0.25 \times 10^{-3}$ mm^2/s
Normal parotid gland	31	20 male/11 female	42.9 ± 16.1 (18-81)	$0.94 \pm 0.18 \times 10^{-3}$ mm^2/s

ADC, apparent diffusion coefficient.

malignant parotid tumor: $0.69 \pm 0.25 \times 10^{-3}$ mm^2/s (Figure 3); and the contralateral normal parotid gland: $0.94 \pm 0.18 \times 10^{-3}$ mm^2/s.

The age distribution of the primary parotid tumor was 42.9 ± 16.1 (18-81) years, of the benign parotid tumor was 39.2 ± 14.5 (18-76) years (Warthin tumor: 55.0 ± 12.8 (39-76) years, pleomorphic adenoma: 33.1 ± 9.8 (18-50) years), and of the malign parotid tumor was 58.3 ± 13.7 (42-81) years.

Gender dispersion of the primary parotid tumor demonstrated a male predominance, as the male-to-female ratio was 20/11, that of the benign parotid tumor was 16/9, that of Warthin tumor was 7/0, that of pleomorphic adenoma was 10/8, and that of the malign parotid tumor was 4/2.

Box plots of ADC mapping of primary parotid tumors and individual aging are shown in Figure 4.

ADC mapping in the primary parotid tumor (Table 2), we found that pleomorphic adenoma had significantly higher ADC value than Warthin tumors ($P < .001$) and malign parotid tumors ($P < .001$). Warthin tumor had a higher ADC value and a statistically significant difference than malign parotid tumor ($P = .007$). The normal parotid gland has a significantly lower ADC value than the pleomorphic adenoma ($P < .001$). Nevertheless, the normal parotid gland ADC value was lower than the Warthin tumor ($P = .176$) and higher than malignant parotid tumors ($P = .146$) but not statistically significant and hence indistinguishable.
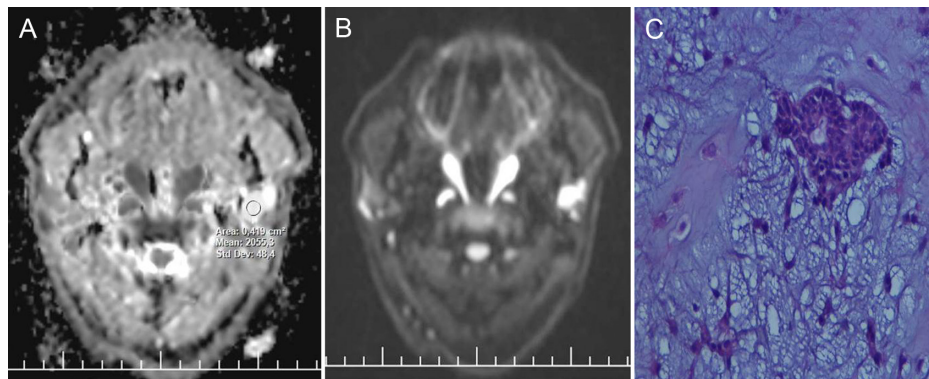
Figure 1. A 42-year-old female with left parotid pleomorphic adenoma. A–C, benign parotid tumor located in deep lobe tumor on axial 3T DW-MR image (A) and ADC mapping (B) and histopathological image (C) myoepithelial cells without atypia are observed on myxoid ground (HE, ×400).
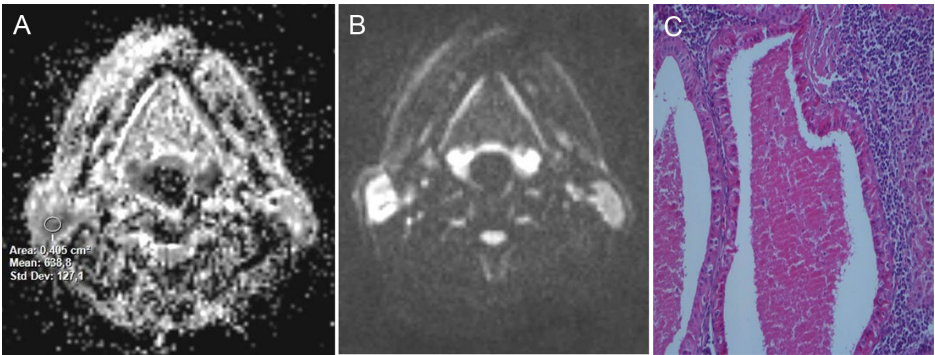
Figure 2. A 69-year-old male with right parotid Warthin tumor. A–C, benign parotid tumor located in superficial lobe on axial 3T DW-MR image (A) and ADC mapping (B) and histopathological image (C) lymphoid stroma, cystic structures covered with oncocytic cells and eosinophilic secretion in the cyst lumen (HE, ×200).
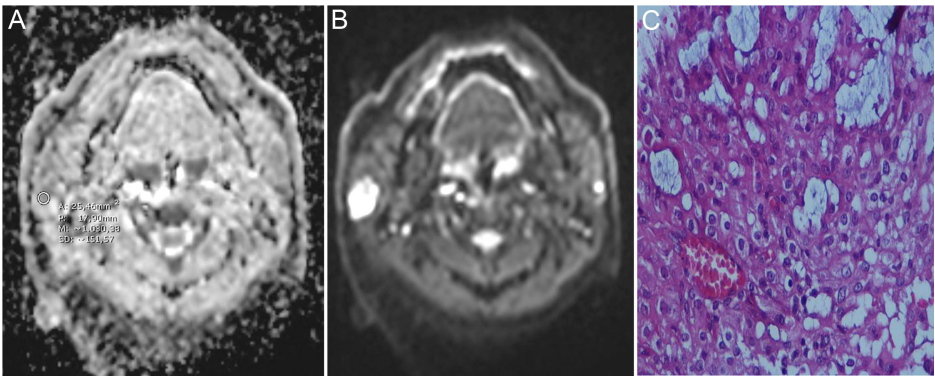
Figure 3. A 58-year-old female with right mucoepidermoid carcinoma. A–C, located in right superficial lobe malignant parotid tumor on axial 3T DW-MR image (A) and ADC mapping (B) and histopathological image (C) mucin-containing tumor tissue consisting of atypical epithelial cells is observed (HE, ×400).
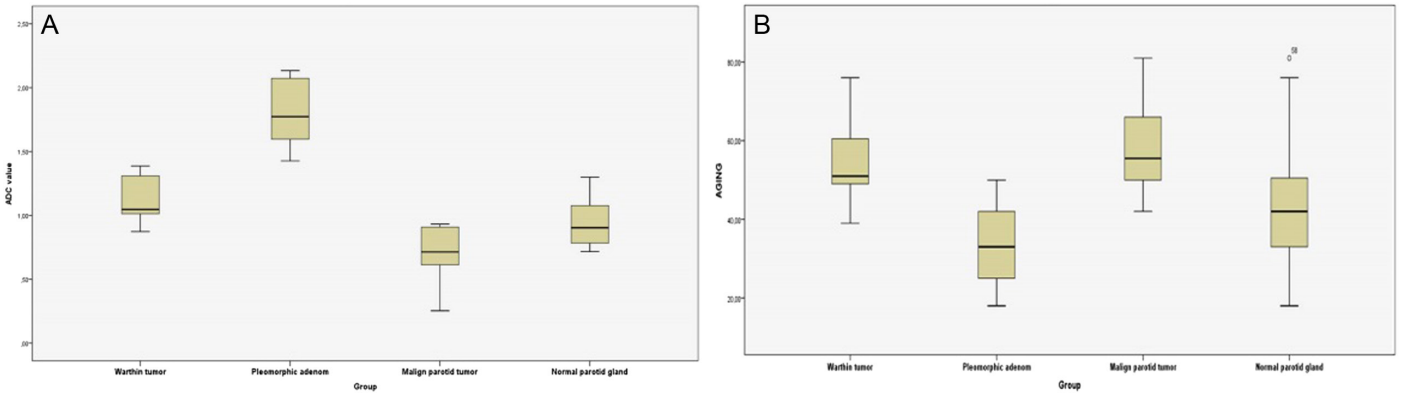
Figure 4. Box plots of apparent diffusion coefficient value (A) and ageing (B) associated with primary parotid tumors: Warthin tumor, pleomorphic adenoma, malignant parotid tumor, and normal parotid gland.

Table 2. Intergroup ADC Comparisons, Post-Hoc Test

Groups	Benign Parotid Tumor	Warthin Tumor	Pleomorphic Adenoma	Malign Parotid Tumor	Normal Parotid Gland
Primer parotid tumor					<0.001
Benign parotid tumor				<0.001	<0.001
Warthin tumor			<0.001	0.007	0.176
Pleomorphic adenoma		<0.001		<0.001	<0.001
Malign parotid tumor	<0.001	0.007	<0.001		0.146

Table 3. Intergroup Age Comparison, Post-Hoc Test

Groups	Benign Parotid Tumor	Warthin Tumor	Pleomorphic Adenoma	Malign Parotid Tumor	Normal Parotid Gland
Primer parotid tumor					<0.001
Benign parotid tumor				0.028	0.667
Warthin tumor			<0.010	0.980	0.243
Pleomorphic adenoma		0.010		0.004	<0.141
Malign parotid tumor	0.028	0.980	0.004		0.117

Table 4. Primary Parotid Tumors, ROC Analysis Between Each Groups

ADC value	Cutoff Value	Sensitivity	Specificity	PPV	NPV	AUC	95% CI
Primer parotid tumor and normal parotid gland	0.93	80	61	67	76	0.79	0.67-0.92
Benign parotid tumor and malign parotid tumor	0.96	96	100	86	100	0.99	0.95-1.00
Pleomorphic adenoma and Warthin tumor	1.41	100	71	90	100	1.00	1.00-1.00
Pleomorphic adenoma and primer parotid tumor	1.37	100	63	62	100	1.00	1.00-1.00
Warthin tumor and primer parotid tumor	0.93	100	72	46	100	0.80	0.57-1.00
Malign parotid tumor and primer parotid tumor	0.96	96	100	40	92	0.98	0.95-1.00
Benign parotid tumor and normal parotid gland	1.34	80	100	91	88	0.93	0.87-1.00
Pleomorphic adenoma and normal parotid gland	1.36	100	100	100	100	1.00	1.00-1.00
Warthin tumor and normal parotid gland	0.98	86	65	35	95	0.76	0.57-0.95
Malign parotid tumor and normal parotid gland	0.75	67	81	40	92	0.78	0.56-0.96

ADC, apparent diffusion coefficient; AUC, area under the curve; NPV, negative predictive value; PPV, positive predictive value; ROC, receiver operating characteristic.

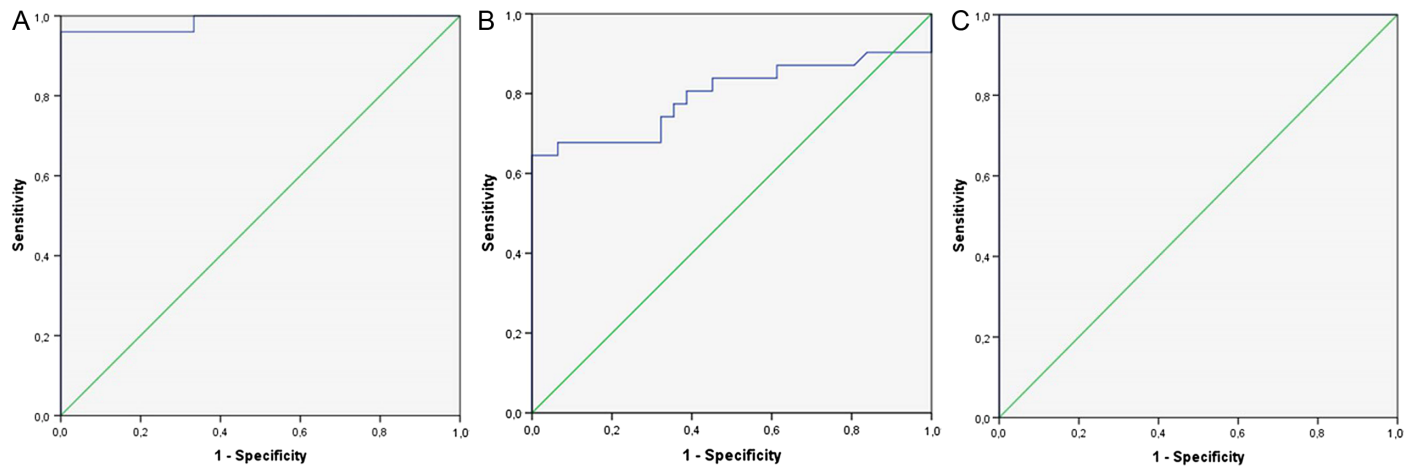**Figure 5.** Receiver operating characteristic analysis graphs in primary parotid tumor—normal parotid gland (A), benign parotid tumor—malignant parotid tumor (**B**), and Warthin tumor—pleomorphic adenoma (C).

With aging in the primary parotid tumor (Table 3), we found that the age of the malign parotid tumor was higher than that of the benign parotid tumor ($P = .028$) and the age of the Warthin tumor was higher age than that of pleomorphic adenoma ($P < .010$).

Gendering in the primary parotid tumor, Warthin tumor had a higher male predominance than pleomorphic adenoma and malign parotid tumor.

Using the distinction performance of ROC analysis in the diagnosis of primary parotid tumors was appreciated. The sensitivity, specificity, positive and negative predictive value, area under the curve (AUC), and 95%CI were evaluated (Table 4). The cutoff value for benign and malignant parotid tumors was 0.96×10^{-3} mm^2/s and that for Warthin tumor and pleomorphic adenoma was 1.41×10^{-3} mm^2/s. The 95% CI) was 0.95-1.00. Sensitivity and specificity were 96% and 100%, respectively, and positive and negative predictive values were 86% and 100%,

respectively (Figure 5). Interobserver correlation for 3T DW-MR imaging and ADC mapping was high (0.96 intraclass coefficient).

DISCUSSION

Among all organs, the parotid gland is the organ with the largest tumor subgroup histopathologically. Tumors often originate from the parotid gland. Salivary gland tumors constituted 3%-12% of head and neck regional tumors and 2%-3% of tumors that can be observed in the whole body.[1] Also, parotid gland tumors are 80% of salivary gland tumors.[27] The most common benign parotid tumors are Warthin tumors and pleomorphic adenoma.[28] The possibility of the primary parotid tumor is 1 of these 2 tumors that should be considered first.[11,29] Pleomorphic adenoma tends to be seen in younger patients than Warthin tumors and malignant parotid tumors.[5] Pleomorphic adenoma is well-circumscribed, encapsulated, and slightly lobulated, containing myxoid, mucoid, and chondroid matrices which provide prominent hyperintense and hypointense heterogenous areas due to the epithelial component on T2W-MR

imaging.[8,23] Pleomorphic adenoma contains various textures, including secretory glands, epithelium, and surrounding fatty stroma.[7] Glandular areas in adenoma and adenoid group tumors can consist of fluid deposits. Causatively, protons move freely in fluid accumulation areas and reflect a high ADC value in pleomorphic adenoma.[16,30]

We peruse the role of 3T DW-MR imaging and ADC mapping in recognizing primary parotid tumor histopathological subtypes. Our study showed that there was a prominent distinction between malignant and benign parotid tumors and within Warthin tumor and pleomorphic adenoma. Pleomorphic adenoma had a higher ADC value than Warthin tumor, malignant parotid tumor, and normal parotid gland. Warthin tumor and malignant parotid tumor might be nearly isointense, indistinguishable from a normal parotid gland on ADC mapping. Aging and gendering might be associated with increasing recognition of primary parotid tumors. The core of our outcomes from this study is using aging and gendering ADC mapping might be a prominent foresight in the differential diagnosis of primary parotid tumors.

The parotid gland has a unique and inhomogeneous texture, which consists of the interstitium and salivary components, and has shown extensive individual variety and changes with aging and gendering.[6,9] The parotid gland indicates a decreasing ADC value due to increased fat aggregation.[19] In a recent study, malignant parotid tumors and the Warthin tumors had been reported to appear isointense to the normal parotid gland on ADC mapping.[9] However, The ADC value of the malignant parotid tumor was lower than the normal parotid gland and the ADC value of the benign parotid tumor and the Warthin tumor was higher than normal parotid gland but it was not statistically significant in our study.

In another study, a small proportion of pleomorphic adenoma was reported to exhibit a typical shiny hyperintensity.[7,16] Nevertheless, primary parotid tumors cannot be diagnosed using routine MR imaging properties.[10,16] Warthin tumor is inclined to be seen in older patients than pleomorphic adenoma with a male predominancy.[5] Warthin tumor is well-edged, unencapsulated, and lobulated, with cystic components and colloid matrices.[30] Warthin tumor consists of rich lymphoid areas, germinal centers, and prominent follicles and exhibits hypercellularity, higher microvesselling, and micronecrotic changes.[3] Hypointensity on DW-MR imaging and ADC mapping is usually observed in the Warthin tumor as well as in malignant parotid tumors.[16,17] No significant difference was observed between Warthin tumor and malignant parotid tumors, so there was overlapping with ADC mapping in most of the study.[1,16]

Malignant parotid tumors can be histopathologically diagnosed according to mitotic activity, cellular anaplasia, necrosis, and neural invasion.[31] Malign parotid tumors, including lymphoma, carcinoma, and carcinosarcoma or mixed tumors, exhibit hypercellularity and limited proton diffusion space of extracellular fields, as a result of restricted DW-MR imaging.[23] Malignant parotid tumors, such as adenoid cystic carcinoma and mucoepidermoid carcinoma, indicate an increased signal intensity reflecting the cystic component due to mucin secretion.[8,17] Malignant parotid tumors exist lower ADC values than Warthin tumors; and also benign parotid tumors exist lower ADC values than Warthin tumors.[5] Cystic carcinoma and pleomorphic adenoma had higher ADC values and overlapping.[10] Therefore, most authors reported that ADC mapping could not discriminate between benign and malignant parotid tumors.[8,16] Carcinosarcoma is a mixed malignant primary parotid tumor, an extremely rare but important subgroup of malignant parotid

tumors characterized by reproducing from pleomorphic adenoma or primarily de novo.[32,33] In contrast to these findings, ADC mapping of malignant parotid tumors was lower than benign parotid tumors in our study, and there was no overlap between malignant and benign parotid tumors.

Lymphoma, which forms an important subgroup of malignant parotid tumors, is characterized by diffuse and abundant infiltration of anaplastic lymphoid cellular in the germinal center and conspicuous follicles.[16,34] The ADC value of lymphoma is lower than carcinomas.[5,17] Lymphoma grouped in malignant parotid tumors with carcinomas in our series has a low ADC value. Therefore, lymphoma and malignant parotid tumors with low ADC values can be distinguishable from benign parotid tumors, including Warthin tumors and pleomorphic adenoma. The ADC mapping of malignant parotid tumors was lower than benign parotid tumors in our study, and there was no overlap between malignant and benign parotid tumors. By the way, we demonstrate that ADC mapping is helpful and can differentiate benign and malignant parotid tumors.

Management of primary parotid tumors is complicated due to their diversity, complex structure, various histopathological subgroups, and even subgroups exhibiting different biological behaviors.[4,11] Preoperative evaluation and deciding the appropriate surgical procedure requires a high-diagnostic technique.[20,33] Routine MR imaging is useful in differential diagnosis and frequently encounters distinctive morphological features.[16,22] Benign parotid tumors and also pleomorphic adenoma markedly hyperintense heterogeneous in T2W-MR imaging.[7,13] Warthin tumors with excess cystic components might resemble pleomorphic adenoma, and smaller cystic components might mimic malignant parotid tumors.[5] Heterogeneous hypointensity with contour irregularity might be facilitates diagnosis in malignant parotid tumors.[1,5] Preoperative differential diagnosis of a primary parotid tumor is important in terms of preoperative surgical planning.[11,35] Benign primary parotid tumors such as Warthin tumors and pleomorphic adenomas are excised with lobectomy, and subtotal parotidectomy, but malign parotid tumors are resected by total parotidectomy.[16,36]

MR imaging assists in determining the signal intensity, boundary, laterality, plurality, location, extension, and invasion of adjacent muscular and fascial parapharyngeal planes and facial nerve for surgical resection planning in primary parotid tumors.[16,34] Magnetic resonance imaging is widely used to differentiate malignant parotid tumors with irregular and vague margins, extraglandular extension, and accompanying lymph nodes.[2,30] Inhomogeneity and hypointensity of T2W MR imaging mostly suggest malignant parotid tumors, but it not sufficient to differentiate diagnosing them alone.[11,23] A benign parotid tumor might be an inhomogeneous nautre resembles malignant parotid tumors.[8] Therefore, the precise diagnosis of a primary parotid tumor with various histopathological subgroups cannot be situated by MR imaging.[1] Contrast-enhanced MR imaging could be used with diagnostic success, but using gadolinium has become lessened in recent years, and there is a need to develop new MR techniques without gadolinium.[1,14]

DW-MR imaging as a functional MR imaging modality might be provide qualitative and quantitative evaluation by demonstrating random movement of protons in a microtexture in routine without gadolinium.[1,16] DW-MR imaging in head and neck have susceptibility artifacts and impaired imaging, swallowing, and movement.[4,14] Using a 3T MR imaging system and a 64-channel head and neck coil with shorter imaging time and higher resolution, it is possible to obtain the optimal

DW-MR imaging and ADC mapping and calculate the ADC value of the parotid gland and primary parotid tumor.[18-24] The ADC value increases with respect to increasing fluid content in the primary parotid tumor.[16] Cystic and necrotic areas and pure cystic tumors might be excluded from ROI, to reflect the histopathology of the primary parotid tumor, and solid areas might be mapped and measured.[10,30] In a recent study, a lower ADC value reflects restricted proton movement in highly cellular areas of Warthin tumors.[5,16] However, in the aforementioned study, the authors included the whole tumor including necrotic cystic areas in the ROI.[3] As we defined, we excluded the cystic necrotic area from ROI to avoid variable ADC mapping. In agreement with these findings, the ADC value of the Warthin tumor was higher than that of the malignant parotid tumors. Therefore, we found that ADC mapping was useful to discriminate benign parotid tumors, including Warthin tumors, from the malignant parotid tumor. In a recent study, the ADC value of malign parotid tumor, Warthin tumor, and pleomorphic adenoma were reported as a $1.04 \pm 0.35 \times 10^{-3}$ mm^2/s, $0.97 \pm 0.35 \times 10^{-3}$ mm^2/s, and $1.74 \pm 0.37 \times 10^{-3}$ mm^2/s.[16] The ADC value in benign parotid tumor was $1.50 \pm 0.48 \times 10^{-3}$ mm^2/s and in malignant parotid tumor was $1.07 \pm 0.29 \times 10^{-3}$ mm^2/s.[23] In a recent study, the primary parotid tumors suggest isointense with normal parotid gland without distinguish of differantial diagnosis.[9] We revealed a little higher ADC value for the Warthin tumor ($1.14 \pm 0.23 \times 10^{-3}$ mm^2/s). Moreover, Warthin tumor has a propensity lower ADC value than pleomorphic adenoma, and higher than the malign parotid tumor. In agreeing with these findings, ADC mapping of the malignant parotid tumor and Warthin tumor was not significantly different from the normal parotid gland we studied. Even so, we noticed that ADC mapping might be helpful to differentiate malign from benign parotid tumors and Warthin tumor and pleomorphic adenomas but not from the normal parotid gland. Using 3T DW-MR imaging and 64-channel head and neck coil, to compose the ADC mapping and using aging and gendering might be useful in differentiate diagnosing from malignant and benign parotid tumors and Warthin tumor and pleomorphic adenoma.

Study Limitations

Our study has several limitations. First, there were limited primary parotid tumors, and therefore only a small number of subgroups of primary parotid tumors were included in the study, but smoking status was not addressed. We included Warthin tumors, pleomorphic adenomas, and malignant primary parotid tumors because malignant parotid tumors were few and heterogeneous, and it is not possible to identify 3T DW-MR imaging and ADC mapping in each subgroup statistically. Second, primary parotid tumor location, growth patterns, margins, signal intensity, cystic and necrotic content, and contrast enhancement were not evaluated, because this study was designed on standard head and neck MR imaging and focused on 3T DW-MR imaging ADC mapping. Thirdly, 3T DW-MR imaging ADC mapping was organized with b-values of 500-1000 sc/mm^2, higher b-values (2000-3000 sc/mm^2) might improve the study. However, there were several studies with conflicting results, and the first report was on qualitative and quantitative evaluation of primary parotid tumors using age, gender, and histopathological data using 3T DW-MR imaging and ADC mapping to characterize primary parotid tumors.

Further prospective studies must be carried out with a high number and wide histopathological subgroup of primary parotid tumors, and this evaluation method of primary parotid tumors using a cutoff value is expected to be an indicator of the distinction of the primary parotid tumor subgroups. Consequently, this research study can aid the relevant literatüre and implies for future research and via emphasizing the 3T DW-MR imaging and ADC mapping, together with aging and gendering, on the distinction of malignant and benign parotid tumors and subgroups, which should be addressed in routine primary parotid tumor imaging protocol.

CONCLUSIONS

In conclusion, our results suggested that 3T DW-MR imaging and ADC mapping with aging and gendering could prominently improve the distinction of malignant and benign parotid tumors including Warthin tumors and pleomorphic adenomas. The ADC mapping of pleomorphic adenoma was significantly higher than that of Warthin tumor and malignant parotid tumor, but the ADC value of Warthin tumor was lower than that of the pleomorphic adenoma and higher than that of malignant parotid tumor. Aging in pleomorphic adenoma was lower when compared to Warthin tumor and malign parotid tumor, gendering in Warthin tumor was male dominance than pleomorphic adenoma and malign parotid tumor. It indicated that the 3T DW-MR imaging and ADC mapping with aging and gendering might be useful in differential diagnosing of malignant and benign parotid tumors, including the Warthin tumors and pleomorphic adenomas.

REFERENCES

1. Karaman CZ, Tanyeri A, Ozgur R. Parotid gland tumors: comparison of conventional and diffusion weighted MR imaging findings with histopathological results. *Turk J Radiol*. 2017;36:60-68.
2. Sumi M, Takagi Y, Uetani M, et al. Diffusion-weighted echoplanar MR imaging of the salivary glands. *AJR*. 2002;178(4):959-965. [CrossRef]
3. Eida S, Sumi M, Sakihama N, Takahashi H, Nakamura T. Apparent diffusion coefficient mapping of salivary gland tumors: prediction of the benignancy and malignancy. *AJNR Am J Neuroradiol*. 2007;28(1):116-121.
4. Yologlu Z, Aydin H, Alp NA, Aribas BK, Kizilgoz V, Arda K. Diffusion weighted magnetic resonance imaging in the diagnosis of parotid masses. Preliminary results. *Saudi Med J*. 2016;37(12):1412-1416. [CrossRef]
5. Wang CW, Chu YH, Chiu DY, et al. JOURNAL CLUB: The Warthin tumor score: a simple and reliable method to distinguish Warthin tumors from pleomorphic adenomas and carcinomas. *AJR*. 2018;210(6):1330-1337. [CrossRef]
6. Inarejos Clemente EJ, Navallas M, Tolend M, et al. Imaging evaluation of pediatric parotid gland abnormalities. *RadioGraphics*. 2018;38(5):1552-1575. [CrossRef]
7. Motoori K, Yamamoto S, Ueda T, et al. Inter- and intratumoral variability in magnetic resonance imaging of pleomorphic adenoma: an attempt to interpret the variable magnetic resonance findings. *J Comput Assist Tomogr*. 2004;28(2):233-246. [CrossRef]
8. Matsushima N, Maeda M, Takamura M, Takeda K. Apparent diffusion coefficients of benign and malignant salivary gland tumors. Comparison to histopathological findings. *J Neuroradiol*. 2007;34(3):183-189. [CrossRef]

9. Matsusue E, Fujihara Y, Matsuda E, et al. Vanishing parotid tumors on MR imaging. *Yonago Acta Med*. 2018;61(1):33-39. [CrossRef]

10. Habermann CR, Arndt C, Graessner J, et al. Diffusion-weighted echo-planar MR imaging of primary parotid gland tumors: is a prediction of different histologic subtypes possible? *AJNR Am J Neuroradiol*. 2009;30(3):591-596. [CrossRef]

11. Thielker J, Grosheva M, Ihrler S, Wittig A, Guntinas-Lichius O. Contemporary management of benign and malignant parotid tumors. *Front Surg*. 2018;5:39. [CrossRef]

12. Awan MS, Ahmad Z. Diagnostic value of fine needle aspiration cytology in parotid tumors. *JMPA*. 2020;54:617-619.

13. Coulter M, Liu J, Marzouk M. Leiomyosarcoma ex pleomorphic adenoma of the parotid gland: a case report and literature review. *Case Rep Otolaryngol*. 2016;2016:9795785. [CrossRef]

14. Metwally Abo El Atta M, Ahmed Amer T, Mohamed Gaballa G, Tharwat Mohammed El-Sayed N. Multi-phasic CT versus dynamic contrast enhanced MRI in characterization of parotid gland tumors. *Egypt J Rad Nucl Med*. 2016;47(4):1361-1372. [CrossRef]

15. Khamis MEM, Ahmed AF, Ismail EI, Bayomy MF, El-Anwar MW. The diagnostic efficacy of apparent diffusion coefficient value and choline/creatine ratio in differentiation between parotid gland tumors. *Egypt J Rad Nucl Med*. 2018;49(2):358-367. [CrossRef]

16. Yerli H, Agildere AM, Aydin E, et al. Value of apparent diffusion coefficient calculation in the differential diagnosis of parotid gland tumors. *Acta Radiol*. 2007;48(9):980-987. [CrossRef]

17. Matsusue E, Fujihara Y, Matsuda E, et al. Differentiating parotid tumors by quantitative signal intensity evaluation on MR imaging. *Clin Imaging*. 2017;46:37-43. [CrossRef]

18. Gatidis S, Graf H, Weiß J, et al. Diffusion-weighted echo planar MR imaging of the neck at 3 T using integrated shimming: comparison of MR sequence techniques for reducing artifacts caused by magnetic-field inhomogeneities. *Magma*. 2017;30(1):57-63. [CrossRef]

19. Srivastava A, Wang J, Zhou H, Melvin JE, Wong DT. Age and gender related differences in human parotid gland gene expression. *Arch Oral Biol*. 2008;53(11):1058-1070. [CrossRef]

20. Direk FK, Deniz M, Uslu AI, Doğru S. Anthropometric analysis of orbital region and age-related changes in adult women. *J Craniofac Surg*. 2016;27(6):1579-1582. [CrossRef]

21. Yerli H, Aydin E, Haberal N, Harman A, Kaskati T, Alibek S. Diagnosing common parotid tumours with magnetic resonance imaging including diffusion weighted imaging vs fine-needle aspiration cytology. *Dentomaxillofac Radiol*. 2010;39(6):349-355. [CrossRef]

22. Tartaglione T, Botto A, Sciandra M, et al. Differential diagnosis of parotid gland tumours: which magnetic resonance findings should be taken in account? *Acta Otorhinolaryngol Ital*. 2015;35(5):314-320. [CrossRef]

23. Srinivasan A, Dvorak R, Perni K, Rohrer S, Mukherji SK. Differentiation of benign and malignant pathology in the head and neck using 3T apparent diffusion coefficient values: early experience. *AJNR Am J Neuroradiol*. 2008;29(1):40-44. [CrossRef]

24. Keil B, Blau JN, Biber S, et al. A 64-channel 3T array coil for accelerated brain MRI. *Magn Reson Med*. 2013;70(1):248-258. [CrossRef]

25. Tao X, Yang G, Wang P, et al. The value of combining conventional, diffusion-weighted and dynamic contrast-enhanced MR imaging for the diagnosis of parotid gland tumours. *Dentomaxillofac Radiol*. 2017;46(6): 20160434. [CrossRef]

26. Yeh CK, Johnson DA, Dodds MW. Impact of aging on human salivary gland function: a community-based study. *Aging (Milano)*. 1998;10(5): 421-428. [CrossRef]

27. Wang J, Takashima S, Takayama F, et al. Head and neck lesions: characterization with diffusion-weighted echo-planar MR imaging. *Radiology*. 2001;220(3):621-630. [CrossRef]

28. Yazici D, Guney Z, Coktu MY, Yildirim I, Arikan OK. Clinicopathological analysis of parotid masses: six-year experience of a tertiary center. *J Pak Med Assoc*. 2020;70(2):308-312. [CrossRef]

29. Verhappen MH, Pouwels PJ, Ljumanovic R, et al. Diffusion-weighted MR imaging in head and neck cancer: comparison between half-Fourier acquired single-shot turbo spin-echo and EPI techniques. *AJNR Am J Neuroradiol*. 2012;33(7):1239-1246. [CrossRef]

30. Okahara M, Kiyosue H, Hori Y, Matsumoto A, Mori H, Yokoyama S. Parotid tumors: MR imaging with pathological correlation. *Eur Radiol*. 2003;13(suppl 4):L25-L33. [CrossRef]

31. Nikitakis NG, Tosios KI, Papanikolaou VS, Rivera H, Papanicolaou SI, Ioffe OB. Immunohistochemical expression of cytokeratins 7 and 20 in malignant salivary gland tumors. *Mod Pathol*. 2004;17(4):407-415. [CrossRef]

32. Jha V, Kolte S, Goyal S. Osteosarcoma arising in carcinosarcoma de novo parotid gland in a young man: an unusual case with review of literature. *J Clin Diagn Res*. 2017;11:8-10. [CrossRef]

33. İncİ E, Hocaoğlu E, Kılıckesmez Ö, Aydin S, Cİmİllİ T. Quantitative diffusion-weighted MR imaging in the differential diagnosis of parotid gland tumors: is it a useful technique? *Turkiye Klinikleri J Med Sci*. 2010;30(4):1339-1345. [CrossRef]

34. Alkan EO, Sarı L, Balsak S, Celik Yabul FC, Altıntaş F, Çoban G. Investigation of the correlation between preoperative diffusion tensor imaging parameters and histopathological findings in patients with meningioma. *Curr Res MRI*. 2022;1(1):15-17. [CrossRef]

35. Teh A, Aswin Kumar A, Teh C, et al. Overview of parotid gland masses. J am osteopath Coll Radiol. 2018;7:5-10.

36. Qian W, Xu XQ, Zhu LN, et al. Preliminary study of using diffusion kurtosis imaging for characterizing parotid gland tumors. *Acta Radiol*. 2019;60(7):887-894. [CrossRef]

Correlation of Qualitative and Quantitative Characteristics of Contrast-Enhanced Dynamic Magnetic Resonance Imaging with Hepatospecific Contrast Agent Gadoxetic Acid (Primovist) and Histopathological Differentiations in Hepatocellular Carcinoma

Kairgeldy Aikimbaev[1] , Hüseyin Tuğsan Ballı[1] , Kıvılcım Eren Erdoğan[2] , Yusuf Can[3] ,
Ferhat Can Pişkin[1] , Sinan Sözütok[1] , Şükrü Mehmet Ertürk[1]

[1]Department of Radiology, Çukurova University, Faculty of Medicine, Adana, Turkey
[2]Department Medical Pathology, Çukurova University, Faculty of Medicine, Adana, Turkey
[3]Department of Radiology, İstanbul Medipol University Hospital, İstanbul, Turkey

Corresponding author: Kairgeldy Aikimbaev, e-mail: aikimbaev@gmail.com

Abstract

Objective: The aim of this study was to investigate the correlation between qualitative and quantitative characteristics of contrast-enhanced dynamic magnetic resonance imaging with hepatospecific contrast agent gadoxetic acid (primovist) and histopathological differentiations in hepatocellular carcinoma.

Methods: This study included 32 consecutive naïve patients with needle biopsy-proven hepatocellular carcinoma. All patients were divided into 2 groups: those with well-differentiated tumors and those with moderately/poorly differentiated tumors. Pre-contrast and post-contrast signal intensities, relative signal intensity ratios, and enhancement ratios of tumors were determined during the hepatobiliary phase of magnetic resonance imaging.

Results: There were no significant differences between 2 groups regarding patients' age ($P = .657$), gender ($P = .589$), chronic hepatitis etiology ($P = .665$), α-fetoprotein levels ($P = .156$), Child-Pugh classes ($P = .166$), contrast-enhancing pattern ($P = .479$), visually registered signal intensities ($P = .228$), and mean pre-contrast relative signal intensity ratios ($P = .444$). Mean post-contrast relative signal intensity ratios and enhancement ratios of well-differentiated tumors were significantly higher compared to moderately/poorly differentiated tumors' values ($P = .017$ and $P = .014$, respectively). The test power of quantitative properties was calculated as good (area under curve for post-contrast relative signal intensity ratio by 0.74, sensitivity by 73%, and specificity by 76%; area under curve for enhancement ratio by 0.71, sensitivity by 82%, and specificity by 76%)).

Conclusion: The quantitative but not qualitative parameters of hepatocellular carcinoma detected during hepatobiliary phase of contrast-enhanced dynamic magnetic resonance imaging with gadoxetic acid (primovist) may provide objective and predictive information in terms of the differentiation between well-differentiated and moderately/poorly differentiated tumors.

Keywords: Contrast agent, gadoxetic acid, primovist, hepatocellular carcinoma, histopathological differentiation, magnetic resonance imaging

INTRODUCTION

Hepatocellular carcinoma (HCC) is the most common primary malignant tumor of the liver and ranks third among cancer-causing cancers.[1] In recent years, with the advances in screening, diagnosis, and treatment methods, the detection frequency of HCC at early stage has increased, and with the application of appropriate treatments, survival times of more than 5 years have been achieved.[2] To predict better treatment results, multivariate statistical analyses were performed and risk factors for possible relapse were investigated. Tumor stage, liver functions, general patient's performance status, tumor biomarkers, and histopathological differentiation of HCC are recognized as main prognostic factors. A needle or surgical biopsy in HCC still provides beneficial information about the morphological variants and subtypes that can serve as important surrogates of tumor behavior for targeted therapies for HCC. Thus, tumor biopsy is being recognized as an invaluable tool for the diagnosis, management, and prognostication of HCC. Moreover, tumor differentiation was included as independent criterion for determining patient selection for liver transplantation in the expanded Toronto criteria.[3] However, currently, tissue biopsies are used less frequently for HCC diagnosis. The main reasons for this tendency are some limitations due to the invasiveness of this procedure such as pain, bleeding, needle tract seeding, possible risk of mortality, and sampling errors along with interpretative errors. On the other hand, HCC is unique among malignancies due to specific tumor characteristics on cross-sectional multiphasic contrast computed tomography (CT) or dynamic magnetic resonance imaging (MRI) that allow for a highly accurate diagnosis of HCC without an invasive biopsy in significant number of patients. Since the histological differentiation of the tumor is widely accepted as important prognostic factor, non-invasive imaging tests are needed to determine the differentiation of the tumor before treatment in HCC patients.

Gadolinium-ethoxybenzyl-diethylenetriamine pentaacetic acid (Gd-EOB-DTPA, Primovist; Bayer AG, Leverkusen, Germany) is used in the routine clinical practice in many radiological departments as a liver-specific contrast agent. Gadolinium-ethoxybenzyl-diethylenetriamine pentaacetic acid , injected intravenously, conjoins in the liver parenchyma with specific organic anion transporting polypeptide (OATP) in the hepatocytes and then excretes through the biliary system and kidney.[4-6] Gadolinium-ethoxybenzyl-diethylenetriamine pentaacetic acid combines futures of dynamic bolus extracellular contrast agent with a delayed hepatobiliary phase;[7] therefore, Gd-EOB-DTPA-enhanced MRI is very sensitive and accurate in the detection of HCC in cirrhotic patients.[8] In MRI examinations performed with Gd-EOB-DTPA contrast agent, the relationships between tumor intensity and histopathological differentiation of the tumor were previously investigated.[9,10] However, these studies are qualitative in their nature and based on visual evaluation.[9,10] Studies with quantitative measurements are few in number, and conflicting results are obtained.[11-15] For this reason, the aim of this study was to investigate the correlation between qualitative and quantitative characteristics of the HCC on dynamic MRI with Gd-EOB-DTPA and histopathological differentiations of the tumors.

METHODS
Study Population
This study was conducted as a single-center retrospective investigation in accordance with the Helsinki Declaration with approval from Çukurova University Medical School Institutional Ethical Committee for Clinical Researches (decision number 7 from April 10, 2020). Written informed consent was obtained from all patients for MRI examination and biopsy before each procedure. This study included 32 consecutive naïve patients (93.7% males, median age 66 years) with HCC histopathologically proven by tru-cut needle biopsy. Inclusion criteria were patient's age above 18 years old, histopathologically proven diagnosis of HCC, and biopsy performed within 1 month after dynamic Gd-EOB-DTPA MRI study. Exclusion criteria were as follows: more than 1-month period between MRI and tissue biopsy, history of previously performed transarterial embolization, thermal ablation therapy or systemic chemotherapy regarding the liver, and reduced iron-laden MRI signal secondary to hemochromatosis or hemosiderin accumulation.

Magnetic Resonance Imaging Protocols
In this study, dynamic MRIs were performed within 1 month before tissue biopsy using 3.0 Tesla scanner (Philips Achieva, Phillips Medical Systems, Best, The Netherlands) with 16-channeled body coil. Dynamic images were obtained as non-contrast phase, arterial phase at 20th

second, portal phase at 70th second, equilibrium phase at 180th second, and hepatobiliary phase at 20th minute after injection of contrast agent. Three-dimensional turbo-field-echo images (T1 high-resolution isotropic volume examination) with parameters determined as TR 3.4 ms, TE 1.8 ms, slice thickness 2 mm, slice spacing 2 mm, matrix size 336×2060, and field of view 320-380 mm were achieved. The contrast agent was injected with a 22 G intravenous catheter inserted into the antecubital vein with a power injector at a rate of 2 mL/s with a dose of 0.025 mmol/kg. After the contrast agent injection, 20-30 mL of 0.9% saline was injected sequentially, at the same rate.

ANALYSIS OF IMAGES
Qualitative Analysis
The MR images were evaluated by 2 radiologists unaware of the results of histopathological analysis with 12 and 6 years of experience in the field of abdominal radiology. All disagreements were resolved by consensus. Analysis of all images was performed at IntelliSpace Portal workstation (Phillips Medical Systems).

In the images obtained, signal intensities (SIs) of the tumor and non-tumor liver parenchyma were visually evaluated. Hepatocellular carcinomas that were visible as hyperintense tumors in the arterial phase (so-called wash-in phenomenon) and hypointense in the portal and/or venous phase (wash-out phenomenon) were considered as lesions with typical contrast pattern. On the other hand, tumors that did not show this specific feature of HCC were considered as lesions with an atypical contrast pattern. In the hepatobiliary phase, the SIs of the tumor and non-tumor liver parenchyma were compared visually. All tumors were divided into 2 groups: hypointense or iso/hyperintense tumors by comparison to the non-tumoral sections of the liver parenchyma.

Quantitative Analysis
Signal intensity measurements were performed with operator-defined region of interest (ROI) of the tumor and liver parenchyma on the pre-contrast and hepatobiliary phase images, corresponding to the same place in both sequences. Region of interest locations were selected from image slices outside of heterogeneous areas, vascular/biliary structures, or necrosis area on pre-contrast slices on the T1-weighted sequences with a round ROI with diameter at least of 1 cm[11] (Figure 1). In addition, the measurement locations for the liver parenchyma were determined to be at least 1 cm away from the tumor. The pre-contrast relative SI ratio (pre-contrast relative signal intensity ratio (RSIR)) and the same parameter during hepatobiliary phase (post-contrast RSIR) from the tumor and non-tumor liver parenchyma with the enhancement ratio (ER) were calculated as follows: RSIR = tumor SI/non-tumor liver parenchyma SI and ER = (post-contrast RSIR−pre-contrast RSIR)/pre-contrast RSIR × 100%, respectively.

Laboratory Tests and Histopathological Evaluation
All patients were evaluated by laboratory tests 1 week before tissue biopsy. Child-Pugh scores and α-fetoprotein (AFP) values were recorded. The biopsies were performed with 16 G tru-cut needle under ultrasound guidance and local anesthesia using 2% prilokain solution. A single sample was taken from the tumor because of possible risk of major complications such as bleeding and needle tract seeding. The material obtained by tissue biopsy was evaluated histopathologically by the pathologist with more than 9 years of experience in the field. All tumors were divided into 2 groups as well-differentiated and moderately/poorly differentiated tumors according to Edmondson and Steiner criteria[15] (Figure 1). The main reason for this approach was that distribution between groups regarding tumor differentiation was not equal (n = 19,

---

MAIN POINTS

- The quantitative but not qualitative parameters of hepatocellular carcinoma detected during hepatobiliary phase of gadolinium-ethoxybenzyl-diethylenetriamine pentaacetic acid (Gd-EOB-DTPA)-enhanced magnetic resonance imaging (MRI) may provide objective and predictive information in terms of the differentiation between well-differentiated and moderately/poorly differentiated tumors.
- Post-contrast relative signal intensity ratio and enhancement ratio on Gd-EOB-DTPA-enhanced MRI provide useful information about histological differentiation of the tumor with high sensitivity and specificity.
- These quantitative metrics can be used in the selection of an optimal candidate for liver transplantation.
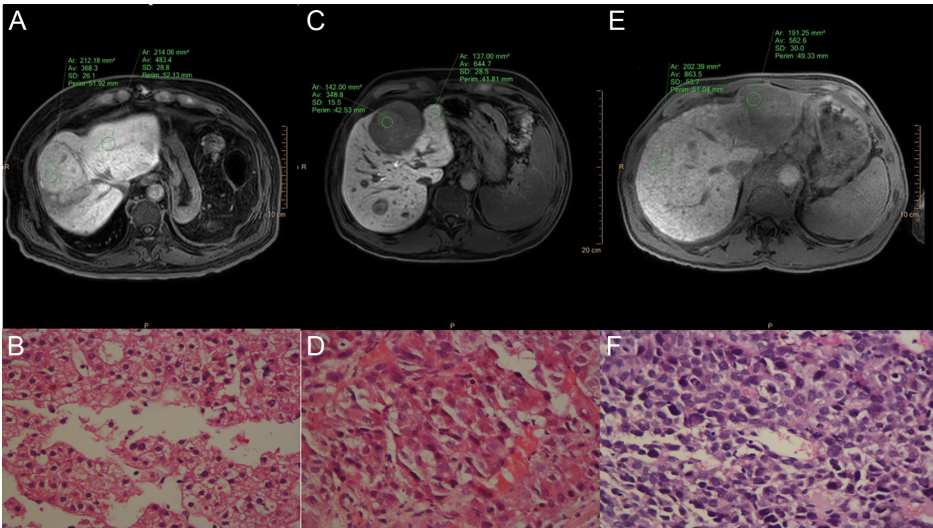
Figure 1. Representative images showing HCC on gadoxetic acid-enhanced dynamic MRI with varied histopathological tumor differentiation. (A) 71-year-old male with well-differentiated HCC. Dynamic MRI shows nodular type of the tumor at the liver segment 8 with post-contrast RSIR 0.75. (B) 71-year-old male with well-differentiated HCC shown on (A). Microscopic imaging shows well-differentiated HCC (hematoxylin and eosin, magnification ×200). (C) 62-year-old male with moderate differentiated HCC. Dynamic MRI shows nodular type of the tumor at the liver segments 4,5, and 8 with post-contrast RSIR 0.53. (D) A 62-year-old male with moderate differentiated HCC shown on (C). Microscopic imaging shows moderate differentiated HCC (hematoxylin and eosin, magnification ×200). (E) 50-year-old male patient with poorly differentiated HCC. Dynamic MRI shows infiltrative type of the tumor at the liver segments 2-4 with post-contrast RSIR 0.63. (F) 50-year-old male patient with poorly differentiated HCC shown on (E). Microscopic imaging shows poorly differentiated HCC (hematoxylin and eosin, magnification ×200). HCC, hepatocellular carcinoma; MRI, magnetic resonance imaging; RSIR, relative signal intensity ratio.

n=9, and n=4 for well-differentiated, moderate, and poor-differentiated HCC, respectively). Provisional performed one-way analysis of variance test with post hoc tests for 3 groups showedn that the group sizes are unequal, and type I error levels are not guaranteed. After splitting all patients into 2 groups, reasonable equality was achieved in terms of the number of patients in this approach (19 patients with well-differentiated vs. 13 patients with moderately/poorly differentiated tumors).

Statistical Analysis

In this study, demographic information and clinical features of patients were expressed with descriptive statistical data. Quantitative data showing normality were presented with mean ± standard deviation, and quantitative data without normality were presented with median and range (minimum–maximum values). Qualitative data were summarized as numbers and percentages. Qualitative features of both groups regarding histopathological differentiation were analyzed with chi-square test with Fischer's exact test, while quantitative parameters were analyzed with Student's t-test. Threshold values for quantitative properties were calculated using the receiver operating characteristic curves. P value <.05 was accepted as statistically significant. Statistical analyses were performed with SStatistical Package for the Social Sciences version 20.0. (IBM SPSS Corp.; Armonk, NY, USA).

RESULTS

Demographic and Clinical Features of the Study Population

In this study, 32 naïve HCC patients (93.7% males) with a median age of 66 years (range, 50-75) were evaluated. The patients' demographic and clinical features are presented in Table 1. Briefly, all patients

Table 1. Demographic and Clinical Characteristics of the Study Population

Parameters	Well-Differentiated HCC	Moderately/Poorly Differentiated HCC	P
Age, years; median (range)	67 (54-74)	65 (50-75)	.657
Sex, n (%)			
Male	13 (86.7)	16 (94.1)	.589
Female	2 (13.3)	1 (5.9)	
Chronic hepatitis etiology, n (%)			
HBV	13 (86.7)	13 (76.5)	.665
HCV	-	3 (17.6)	
Cryptogenic	2 (13.3)	1 (5.9)	
α-fetoprotein, n (%)			
≤ 20 (ng/mL)	9 (60.0)	6 (35.3)	.156
> 20 (ng/mL)	6 (40.0)	11 (64.7)	
Child-Pugh class, n (%)			
A	11 (73.3)	8 (47.1)	.166
B	4 (26.7)	9 (52.9)	

HCC, hepatocellular carcinoma; HBV, hepatitis B virus; HCV, hepatitis C virus.

Chi-square test with Fischer's exact test.

Table 2. Qualitative Findings of Gadoxetic Acid-Enhanced Dynamic MRI in the Study Population

Parameters	Well-Differentiated HCC	Moderately/Poorly Differentiated HCC	*P*
Tumor size, mm; median (range)	77 (57-97)	83 (64-102)	.649
Enhancement pattern, n (%)			
Typical	7 (58.8)	7 (53.8)	.479
Non-typical	6 (42.2)	6 (47.2)	
Hepatobiliary phase SI, n (%)			
Hypointense	15 (78.9)	12 (92.3)	.228
Iso/hyperintense	4 (21.1)	1 (7.7	

MRI, magnetic resonance imaging; HCC, hepatocellular carcinoma; SI, signal intensity.

Chi-square test with Fischer's exact test.

had clinically proven chronic hepatitis supported by laboratory tests. Chronic hepatitis etiologies included hepatitis B virus (n=26; 81.4%), hepatitis C virus (n=3; 9.3%), and cryptogenic (n=3, 9.3%). At the time of diagnosis, AFP values of 15 (46.9%) patients were ≤20 ng/mL and AFP values of remaining patients (n=17; 53.1%) were >20 ng/mL. Patients were in the Child-Pugh class A or B (n=13; 46.6% and n=19; 53.4%, respectively). As a result of histopathological evaluation of the lesions, 19 (59.3%) well-differentiated and 13 (41.7%) moderately/poorly differentiated tumors were detected.

There were no statistically significant differences between 2 groups regarding patients' age (P = .657), gender (P=.589), chronic hepatitis etiology (P = .665), AFP levels (P = .156), and Child-Pugh classes (P = .166).

Qualitative Magnetic Resonance Imaging Findings
When contrasting pattern of the tumors was evaluated in contrast-enhanced MRI, typical enhancement pattern (so-called wash-in followed by wash-out) was detected in 11 (58.8%) patients with well-differentiated tumors and atypical enhancement pattern in 8 (42.2%)

patients from the same group. On the other hand, 7 (53.8%) patients with the moderately/poorly differentiated tumors had a typical contrast pattern, while remaining 6 (47.2%) patients had the atypical contrast pattern. There was no significant difference between the contrasting pattern of the 2 groups (P = .479). When SIs of the tumors and liver parenchyma were compared during the hepatobiliary phase of dynamic MRI, most of the well-differentiated tumors (n=15, 78.9%) had hypointense SIs relative to the liver parenchyma and 4 (21.1%) were iso- or hyperintense. Additionally, SIs of moderately/poorly differentiated tumors were hypointense in 12 (92.3%) patients and iso-or hyperintense in 1 (7.7%) patient compared to adjacent liver parenchyma. There was no statistically significant difference between the SIs during hepatobiliary phase of 2 groups (P = .228). Qualitative MRI findings of tumors, contrasting patterns, and SIs at the hepatobiliary phase are summarized in Table 2.

Quantitative Magnetic Resonance Imaging Findings
The mean values of the pre-contrast RSIR of the tumors were 0.76 ± 0.12 for well-differentiated tumors and 0.71 ± 0.22 for moderately/poorly
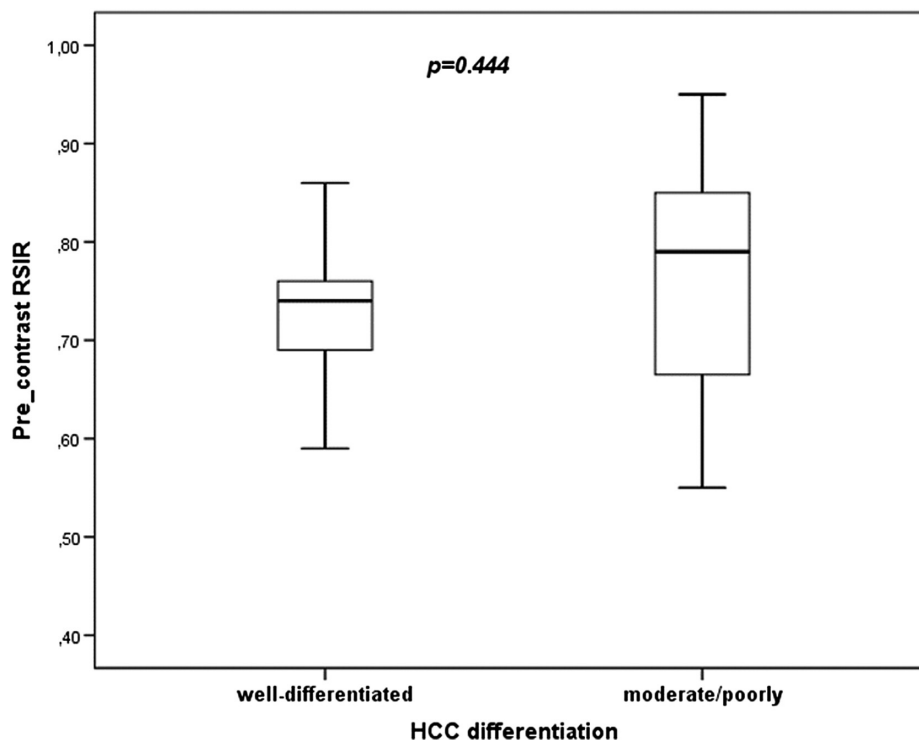

Figure 2. Relationship between pre-contrast RSIR and HCC differentiation in patient population. Student's t-test shows no difference between well-differentiated and moderately/poorly differentiated HCC in study population (P = .444). RSIR, relative signal intensity ratio; HCC, hepatocellular carcinoma.
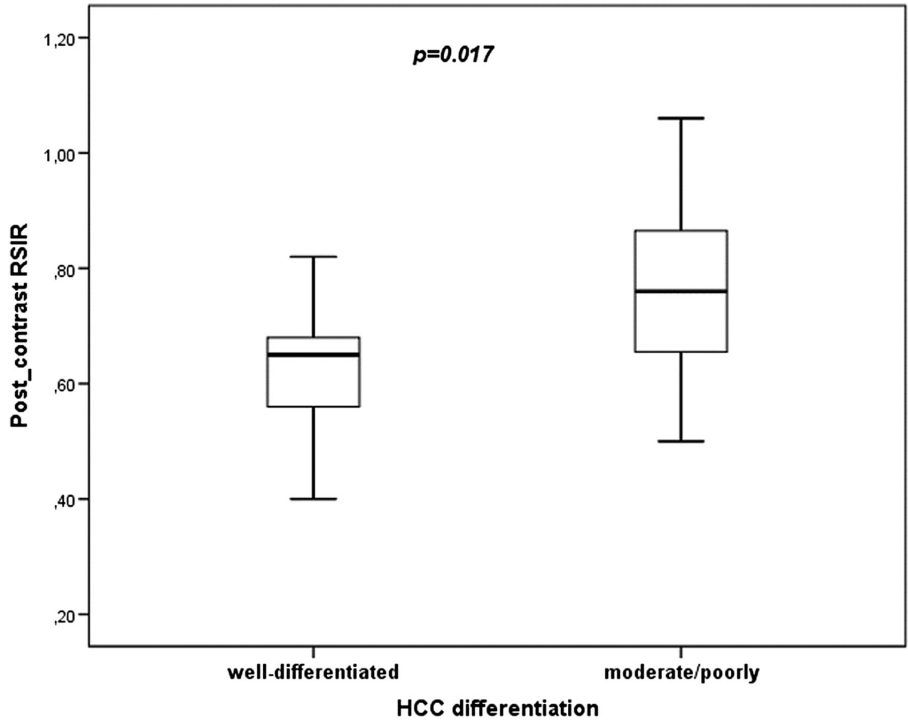
Figure 3. Relationship between post-contrast RSIR and HCC differentiation in patient population. Student's t-test shows statistically significant difference between well-differentiated and moderately/poorly differentiated HCC's post-contrast RSIR values in study population (P = .017). RSIR, relative signal intensity ratio, HCC, hepatocellular carcinoma.

differentiated tumors. There was no significant difference between the mean pre-contrast RSIR values between 2 groups (*P* = .444) (Figure 2). The mean values of the post-contrast RSIRof the tumors were 0.74 ± 0.19 and 0.58 ± 0.17 for well-differentiated tumors and for moderately/poorly differentiated tumors, respectively. Mean ER values of tumors were 89.8 ± 60.55 for well-differentiated tumors and 47.7 ±
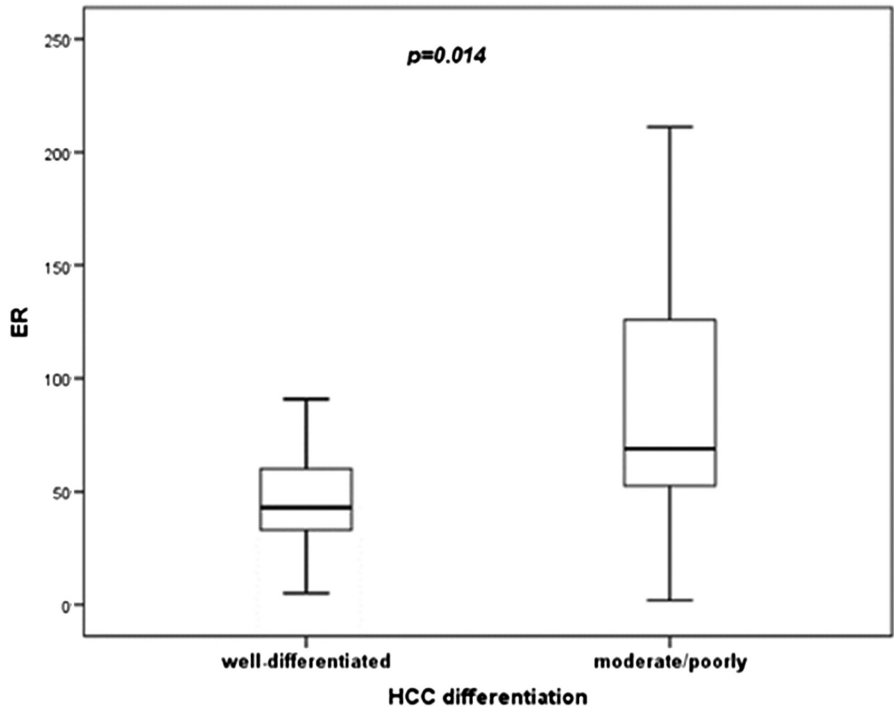

Figure 4. Relationship between ER and HCC differentiation in patient population. Student's t-test shows statistically significant difference between well-differentiated and moderately/poorly differentiated HCC's ER values in study population (P = .014). ER, enhancement ratio, HCC, hepatocellular carcinoma

Table 3. Quantitative Findings on Gd-EOB-DTPA-Enhanced Dynamic MRI in the Study Population

Parameters, Mean ± SD	Well-Differentiated HCC	Moderately/Poorly Differentiated HCC	P
Pre-contrast RSIR	0.76 ± 0.12	0.71 ± 0.22	.044
Post-contrast RSIR	0.74 ± 0.19	0.58 ± 0.17	.017
ER	89.8 ± 60.55	47.7 ± 25.8	.014

Gd-EOB-DTPA, gadolinium-ethoxybenzyl-diethylenetriamine pentaacetic acid; MRI, magnetic resonance imaging; SD, standard deviation; HCC, hepatocellular carcinoma; RSIR, relative signal intensity ratio; ER, enhancement ratio.

Student's *t*-test.

25.8 for moderately/poorly differentiated tumors. Mean post-contrast RSIR and ER valuesof well-differentiated tumors were statistically significantly higher compared to the mean post-contrast RSIR and ER valuesof moderately/poorly differentiated tumors ($P = .017$ and $P = .014$, respectively) (Figures 3 and 4, respectively). Quantitative MRI findings, contrasting patterns, and SIs during hepatobiliary phase are summarized in the Table 3.

DISCUSSION

Tumor differentiation of HCC is a well-known independent factor directly representing the prognosis of the disease detected at the time of diagnosis. Tamura et al[16] analyzed the clinicopathological information of 53 patients who underwent liver transplantation due to HCC and found that the risk of recurrence after treatment was directly connected to the tumor differentiation. Later, tumor differentiation was included as an independent criterion for determining patient selection for liver transplantation in the expanded Toronto criteria.[3] In the present study, regarding the histopathological differentiation of HCCs, tumors were divided into 2 groups as well-differentiated and moderately/poorly differentiated due to the fact that moderately/poorly differentiated tumors have much worse prognosis.[17] Qualitative and quantitative characteristics of the 2 groups determined on MRI with Gd-EOB-DTPA at the time of the diagnosis were evaluated. While there was no difference between the qualitative characteristics of the 2 groups with different tumor differentiation, a significant difference between the quantitative features between the values of post-contrast RSIR and ER was detected ($P = .017$ and $P = .014$, respectively).

According to the American Association for the Study of Liver Diseases guidelines,[18] in cirrhotic patients, hyperatenuation/hyperintensity during arterial phase, and hypoatenuation/hypointensity during portal and/or venous phase in tumors larger than 1 cm on dynamic CT or MRI is sufficient for the diagnosis of HCC. On the other hand, the sensitivity of this typical contrast enhancement pattern for diagnosis was determined to be variable and limited (33%-81.8%).[2,15] In the study by Leoni et al[19] 204 HCCs with a pathologically proven <3 cm nodule were evaluated visually in terms of the contrast pattern. Typical contrasting pattern was detected in 47% (47/101) of all HCCs. In addition, moderately and poorly differentiated tumors showed a significantly more frequent typical contrast pattern than well-differentiated tumors (48% (67/141) vs. 13% (8/63)). In this study, 43.7% (14/32) of tumors showed a typical contrast-enhancing pattern and the rates were consistent with the previously published data.[20,21] There was no difference in terms of frequency of showing typical contrast enhancement pattern of well-differentiated and moderately/poorly differentiated tumors ($P = .479$). This may be because the typical contrast enhancement pattern does not fully reflect tumor differentiation. The relationship between tumor carcinogenesis steps and tumor vascularity of HCCs was previously investigated; it was determined that the tumor has blood supply from the both arterial and portal system in early carcinogenesis stages

and that the tumor has blood supply only from the arterial system in the advanced carcinogenesis stages. These changes in the blood supply determine the contrast pattern of the tumor in dynamic CT and MR imaging.[22,23] For this reason, we think that the typical contrast enhancement pattern detected in CT/MRI may be a predictive marker for moderate/poor histological differentiation of tumors, although its sensitivity is limited in HCC patients.

Gadolinium-ethoxybenzyl-diethylenetriamine pentaacetic acid is a paramagnetic liver-specific contrast agent. Previously published studies showed that Gd-EOB-DTPA at the hepatobiliary phase increased the sensitivity of early detection of HCCs compared to other contrast agents. Due to the fact that hepatocytes and HCC cells have different Gd-EOB-DTPA uptakes, tumors during the hepatobiliary phase are detected mostly as hypointense compared to background liver parenchyma. Therefore, HCCs can be easily detected visually in the hepatobiliary phase.[24,25] However, in later studies, it was found that all HCCs were not hypointense in the hepatobiliary phase, and some tumors showed iso- or hyperintense features. In the systematic review by Erra et al.[26] 13% (418/3110) of pathologically proven HCCs detected in MRI with Gd-EOB-DTPA showed iso- or hyperintense properties. In the study by Choi et al.[6] it was determined that in the tumors detected during hepatobiliary phase as hypointense, histological differentiation was poor and the risk of recurrence was higher. Chang et al[27] found that low post-contrast RSIR values on MRI performed with Gd-EOB-DTPA are predictive markers for poor histological differentiation of the tumor. In the study by Jin et al.[28] in the hepatobiliary phase on MRI with Gd-EOB-DTPA, ER values of well-differentiated tumors were significantly higher compared to moderately/poorly differentiated tumors ($P < .01$).

In this study, in the visual (qualitative) evaluation performed in the hepatobiliary phase, no difference between the signal intensity characteristics of the well-differentiated and moderately/poorly differentiated tumors was detected. However, there was a significant difference between the quantitative parameters of the well-differentiated and moderately/poorly differentiated tumors ($P = .017$ for post-contrast RSIR and $P = .014$ for ER). Gadolinium-ethoxybenzyl-diethylenetriamine pentaacetic acid is taken into hepatocytes through specific OATP-8 proteins located in the cell membranes. In the study by Kitao et al.[29] it was determined that as the HCC tumor carcinogenesis steps progress, OATP-8 expression in the cell membrane decreases. Therefore, moderately and poorly differentiated tumors show lower signal characteristics in MRI with Gd-EOB-DTPA than well-differentiated tumors. We think that the qualitative assessment made in MRI with Gd-EOB-DTPA is open to errors because of its subjective nature. Moreover, post-contrast RSIR and ER value differences in HCC during hepatobiliary phase lead to conclusion that quantitative evaluation could be an objective predictive marker for tumor differentiation. Our findings are in accordance with results of the study of Chang et al.[27]
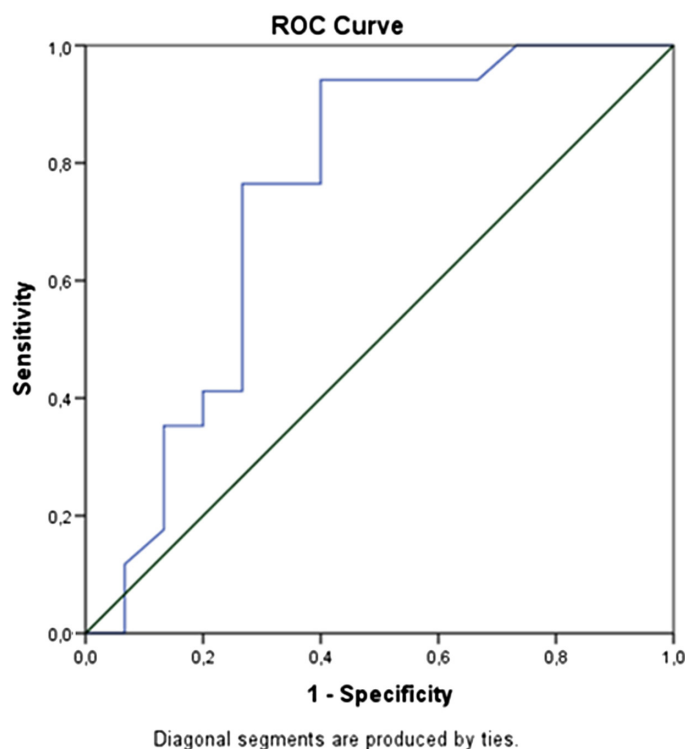
Figure 5. Area under curve for post-contrast RSIR in study population. ROC analysis shows good test power of post-contrast RSIR for the separation of well-differentiated and moderate/poorly differentiated tumors (area under curve 0.74, sensitivity 73%, and specificity 76%). RSIR, relative signal intensity ratio.

which determined post-contrast RSIR threshold values to differentiate other tumors from poorly differentiated tumors; sensitivity was 81.4% and specificity was 93.9% for this test. In this study, the test power of quantitative properties for the threshold values determined for the separation of well-differentiated and moderately/poorly differentiated tumors was calculated as good (area under curve for post-contrast RSIR = 0.74, sensitivity = 73%, and specificity = 76%; area under curve for ER = 0.71, sensitivity = 82%, and specificity = 76%) (Figures 5 and 6, respectively).

There were some important limitations in this study. First, this investigation was conducted retrospectively although we included all consecutive patients with histologically proven HCC in the study. Since this study was a retrospective, sufficient sample size was not calculated. Another important limitation is due to the relatively small number of patients because routine biopsies unfortunately are not commonly done due to possible complications of this procedure. Nevertheless, the number of patients is not significantly less compared to many other published studies. In order for the number of tumors examined in groups to be similar, moderately and poorly differentiated tumor diffraction was handled within the same group, but it may have affected study results. Another important limitation is that histopathological examinations were performed on the single specimen obtained by tru-cut biopsy. Thus, the presence of different tumor diffraction sites in the investigated tumor was ignored. Although there were no patients with Child-Pugh Class C in the groups, the effect of impaired liver function on the enhancement pattern and amount of contrast agent involvement was neglected in cirrhotic patients.
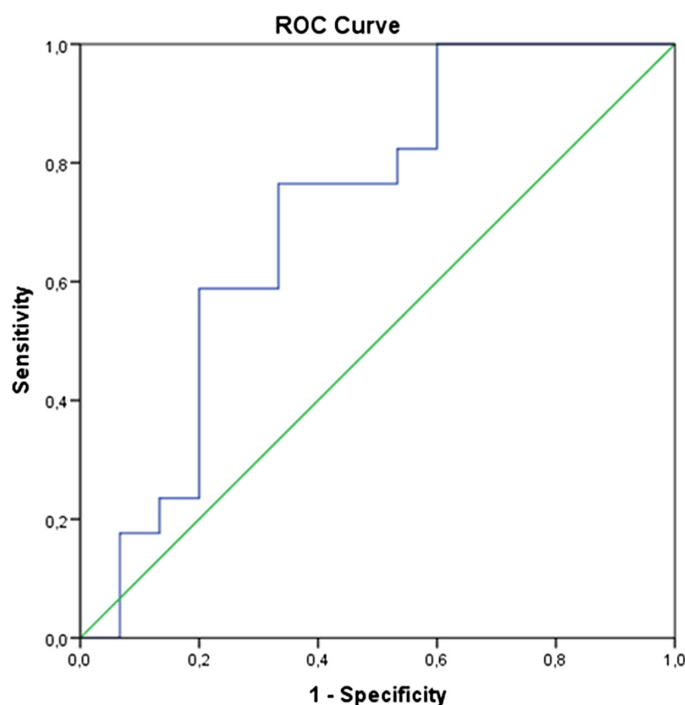

Figure 6. Area under curve for ER in study population. ROC analysis shows good test power of ER for the separation of well-differentiated and moderate/poorly differentiated tumors (area under curve for ER 0.71, sensitivity 82%, and specificity 76%). ER, enhancement ratio.

In conclusion, the quantitative but not qualitative parameters of HCC detected during hepatobiliary phase of Gd-EOB-DTPA-enhanced MRI may provide objective and predictive information in terms of the differentiation between well-differentiated and moderately/poorly differentiated tumors. Post-contrast RSIR and ER on Gd-EOB-DTPA-enhanced MRI provide useful information about histological differentiation of the tumor with high sensitivity and specificity. These quantitative metrics can be used in the selection of an optimal candidate for liver transplantation. Further studies with standardized quantitative protocols and pre-calculated sample size are needed to clarify the exact threshold values for tumor differentiation in HCC.

REFERENCES
1. Bray F, Ferlay J, Soerjomataram I, Siegel RL, Torre LA, Jemal A. Global cancer statistics 2018: GLOBOCAN estimates of incidence and mortality

worldwide for 36 cancers in 185 countries. *CA Cancer J Clin*. 2018; 68(6):394-424. [CrossRef]

2. Kudo M, Izumi N, Sakamoto M, et al. Survival Analysis over 28 years of 173,378 Patients with Hepatocellular Carcinoma in Japan. *Liver Cancer*. 2016;5(3):190-197. [CrossRef]

3. Sapisochin G, Goldaracena N, Laurence JM, et al. The extended Toronto criteria for liver transplantation in patients with hepatocellular carcinoma: A prospective validation study. *Hepatology*. 2016;64(6):2077-2088. [CrossRef]

4. Schuhmann-Giampieri G, Schmitt-Willich H, Press WR, Negishi C, Weinmann HJ, Speck U. Preclinical evaluation of Gd-EOB-DTPA as a contrast agent in MR imaging of the hepatobiliary system. *Radiology*. 1992;183(1):59-64. [CrossRef]

5. Vogl TJ, Kümmel S, Hammerstingl R, et al. Liver tumors: comparison of MR imaging with Gd-EOB-DTPA and Gd-DTPA. *Radiology*. 1996;200(1): 59-67. [CrossRef]

6. Narita M, Hatano E, Arizono S, et al. Expression of OATP1B3 determines uptake of Gd-EOB-DTPA in hepatocellular carcinoma. *J Gastroenterol*. 2009;44(7):793-798. [CrossRef]

7. Frericks BB, Loddenkemper C, Huppertz A, et al. Qualitative and quantitative evaluation of hepatocellular carcinoma and cirrhotic liver enhancement using Gd-EOB-DTPA. *AJR*. 2009;193(4):1053-1060. [CrossRef]

8. Baird AJ, Amos GJ, Saad NF, Benson MD. Retrospective audit to determine the diagnostic accuracy of Primovist-enhanced MRI in the detection of hepatocellular carcinoma in cirrhosis with explant histopathology correlation. *J Med Imaging Radiat Oncol*. 2013;57(3):314-320. [CrossRef]

9. Lee MH, Kim SH, Park MJ, Park CK, Rhim H. Gadoxetic acid-enhanced hepatobiliary phase MRI and high-b-value diffusion-weighted imaging to distinguish well-differentiated hepatocellular carcinomas from benign nodules in patients with chronic liver disease. *AJR*. 2011;197(5):W868-W875. [CrossRef]

10. Kobayashi S, Matsui O, Gabata T, et al. Relationship between signal intensity on hepatobiliary phase of gadolinium ethoxybenzyl diethylene triaminepentaacetic acid (Gd-EOB-DTPA)-enhanced MR imaging and prognosis of borderline lesions of hepatocellular carcinoma. *Eur J Radiol*. 2012;81(11):3002-3009. [CrossRef]

11. Kogita S, Imai Y, Okada M, et al. Gd-EOB-DTPA-enhanced magnetic resonance images of hepatocellular carcinoma: correlation with histological grading and portal blood flow. *Eur Radiol*. 2010;20(10):2405-2413. [CrossRef]

12. Okada M, Imai Y, Kim T, et al. Comparison of enhancement patterns of histologically confirmed hepatocellular carcinoma between gadoxetate- and ferucarbotran-enhanced magnetic resonance imaging. *JMRI*. 2010;32(4):903-913. [CrossRef]

13. Choi JY, Kim MJ, Park YN, et al. Gadoxetate disodium-enhanced hepatobiliary phase MRI of hepatocellular carcinoma: correlation with histological characteristics. *AJR*. 2011;197(2):399-405. [CrossRef]

14. Kim HY, Choi JY, Kim CW, et al. Gadolinium ethoxybenzyl diethylenetriamine pentaacetic acid-enhanced magnetic resonance imaging predicts the histological grade of hepatocellular carcinoma only in patients with Child-Pugh class A cirrhosis. *Liver Transpl*. 2012;18(7):850-857. [CrossRef]

15. Edmondson HA, Steiner PE. Primary carcinoma of the liver: a study of 100 cases among 48,900 necropsies. *Cancer*. 1954;7(3):462-503. [CrossRef]

16. Tamura S, Kato T, Berho M, et al. Impact of histological grade of hepatocellular carcinoma on the outcome of liver transplantation. *Arch Surg*. 2001;136(1):25-30. [CrossRef]

17. Choi JW, Lee JM, Kim SJ, et al. Hepatocellular carcinoma: imaging patterns on gadoxetic acid-enhanced MR Images and their value as an imaging biomarker. *Radiology*. 2013;267(3):776-786. [CrossRef]

18. Sherman M. The radiological diagnosis of hepatocellular carcinoma. *Am J Gastroenterol*. 2010;105(3):610-612. [CrossRef]

19. Leoni S, Piscaglia F, Golfieri R, et al. The impact of vascular and non-vascular findings on the noninvasive diagnosis of small hepatocellular carcinoma based on the EASL and AASLD criteria. *Am J Gastroenterol*. 2010;105(3):599-609. [CrossRef]

20. Yoon SH, Lee JM, So YH, et al. Multiphasic MDCT enhancement pattern of hepatocellular carcinoma smaller than 3 cm in diameter: tumor size and cellular differentiation. *AJR*. 2009;193(6):W482-W489. [CrossRef]

21. Lee JH, Lee JM, Kim SJ, et al. Enhancement patterns of hepatocellular carcinomas on multiphasic multidetector row CT: comparison with pathological differentiation. *Br J Radiol*. 2012;85(1017):e573-e583. [CrossRef]

22. Honda H, Tajima T, Kajiyama K, et al. Vascular changes in hepatocellular carcinoma: correlation of radiologic and pathologic findings. *AJR*. 1999;173(5):1213-1217. [CrossRef]

23. Liu GJ, Xu HX, Lu MD, et al. Correlation between enhancement pattern of hepatocellular carcinoma on real-time contrast-enhanced ultrasound and tumour cellular differentiation on histopathology. *Br J Radiol*. 2007;80(953):321-330. [CrossRef]

24. Golfieri R, Renzulli M, Lucidi V, Corcioni B, Trevisani F, Bolondi L. Contribution of the hepatobiliary phase of Gd-EOB-DTPA-enhanced MRI to Dynamic MRI in the detection of hypovascular small (≤ 2 cm) HCC in cirrhosis (</=2 cm) HCC in cirrhosis. *Eur Radiol*. 2011;21(6):1233-1242. [CrossRef]

25. Inoue T, Kudo M, Komuta M, et al. Assessment of Gd-EOB-DTPA-enhanced MRI for HCC and dysplastic nodules and comparison of detection sensitivity versus MDCT. *J Gastroenterol*. 2012;47(9):1036-1047. [CrossRef]

26. Erra P, Puglia M, Ragozzino A, et al. Appearance of hepatocellular carcinoma on gadoxetic acid-enhanced hepato-biliary phase MR imaging: a systematic review. *Radiol Med*. 2015;120(11):1002-1011. [CrossRef]

27. Chang WC, Chen RC, Chou CT, et al. Histological grade of hepatocellular carcinoma correlates with arterial enhancement on gadoxetic acid-enhanced and diffusion-weighted MR images. *Abdom Imaging*. 2014; 39(6):1202-1212. [CrossRef]

28. Jin YJ, Cho SG, Lee KY, Kim JM, Lee JW. Association between relative liver enhancement on gadoxetic acid enhanced magnetic resonance images and histologic grade of hepatocellular carcinoma. *Medicine*. 2017;96(30):e7580. [CrossRef]

29. Kitao A, Matsui O, Yoneda N, et al. Gadoxetic acid-enhanced MR imaging for hepatocellular carcinoma: molecular and genetic background. *Eur Radiol*. 2020;30(6):3438-3447. [CrossRef]

Magnetic Resonance Measurement of Lateral Ventricular Diameters in Cases of Colpocephaly and Corpus Callosum Agenesis

Önder Durmaz , Erdem Fatihoğlu , Ali Osman Gülmez

Department of Radiology, Erzincan Binali Yıldırım University, Faculty of Medicine, Erzincan, Turkey

Abstract

Objective: One of the most typical brain anomalies seen in humans is agenesis of the corpus callosum. Its estimated prevalence in the general population is 3-7 per 1000. Apart from the absence of the corpus callosum, one of the most common symptoms is colpocephaly. In this study, we aimed to measure the lateral ventricle diameters by magnetic resonance imaging in cases of colpocephaly secondary to corpus callosum agenesis.

Methods: Patients diagnosed with colpocephaly secondary to corpus callosum agenesis between January 2005 and December 2021 were re-evaluated in retrospective scans. The patients' age, gender, and their measurement values in the magnetic resonance examination were noted.

Results: The study was carried out with 90 patients who met the criteria. It was found that if the occipital horn of the lateral ventricle is over 20 mm and the other horns are smaller than 7 mm, it can predict the presence of colpocephaly with a sensitivity of 94% and a specificity of 95% (area under the curve=0.728).

Keywords: Agenesis, corpus callosum, lateral ventricle

INTRODUCTION

The band of over 200 million nerve fibers known as the corpus callosum joins the left and right cerebral hemispheres. The rostrum, genu, anterior midbody, isthmus, and splenium have historically been considered to comprise the corpus callosum's 5 different components. The main function of the corpus callosum is to allow interhemispheric transmission utilizing both inhibitory and excitory mechanisms.[1] It begins to mature through a difficult process of neuronal migration and development around the 12th week of pregnancy. By week 20, fetal magnetic resonance imaging (MRI) or an ultrasound examination can detect the corpus callosum. As with most brain structures, the corpus callosum is thought to be fully developed at age 4, but it probably continues to evolve over the years.[2,3] Agenesis of the corpus callosum (CCA) is one of the most frequent brain abnormalities seen in humans. Its prevalence is estimated to range from 3 to 7 per 1000 live births in the general population, depending on diagnostic methods and sample groups. Colpocephaly is one of the indispensable criteria in CCA.[4] Although there are many studies measuring lateral ventricular diameters in the literature, there is no measurement in cases of corpus callosum and colpocephaly. In this study, we aimed to measure the lateral ventricle diameters in adult patients with corpus callosum agenesis and colpocephaly.

METHODS

The Institutional Review Board gave its approval for this retrospective investigation. Because this was a retrospective study, informed consent was not required (ethics committee number: 43576249-502.01.02-E.40336, date: July 10, 2022, Erzincan Binali Yıldırım University).

Between January 2005 and December 2021, the hospital medical archive was retrospectively scanned for the words "colpocephaly" and "corpus callosum agenesis." Patients younger than 18 years of age were excluded from the study, but no other exclusion criteria were applied. Measurements were carried out in the 1.5 T magnetic resonance (MR) system (Magnetom Aera, Siemens Healthcare, Erlanger, Germany) cranial MR examination using standard T2 axial images (slice thickness is 5 mm, FoV read is 220 mm, FoV phase is 100%, voxel size:0.7 × 0.7 × 5 mm dist factor is 20%, the repetition time 5600 ms and time of echo 103 ms, and averages are 1). While the measurements in the frontal and temporal horns were made 5 mm deep at the farthest distance, the measurements in the occipital horns were made from the widest part. Measurements were made only in axial sections in the transverse plane. Examples of measurements taken are schematized in Figures 1-3.

The instrument used to analyze the study's data was the Statistical Package for the Social Sciences (SPSS) for Windows 20 (IBM SPSS Inc., Chicago, Ill, USA). The normal distribution of the data was confirmed by the Kolmogorov–Smirnov test. The mean and standard deviation of numerical data with a normally distributed distribution are shown. Data that do not have a normal distribution are shown using the median. The Mann–Whitney U test and the Student's t-test were used to compare numerical variables between groups. Pearson and Spearman correlation analyses were used to look for any relationships between the variables. Positive predictive value, negative predictive value, and receiver operating
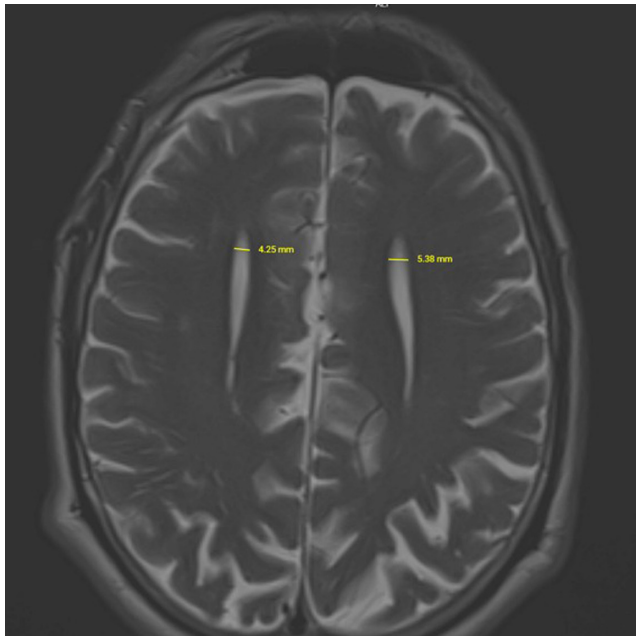
Figure 1. The measurement of the frontal horns of the lateral ventricles in a 40-year-old male patient with colpocephaly and agenesis of the corpus callosum is schematized. The measurements were 4.25 mm on the right and 5.38 on the left in both lateral ventricles.

characteristic (ROC) analyses were used to assess the effectiveness of the investigated diagnostic techniques. $P = .05$ was considered as the statistically significant value.

RESULTS

About 108 patients who met the criteria were found, and since the images of 18 of them could not be accessed, 90 patients remained. The mean age was calculated as 40 (range: 18-64 years). Fifty of the patients (55%) were men and 40 were women (45%). In cases with corpus callosum, no significant difference was observed between the 2 groups in terms of gender ($P > .05$). The lateral ventricle frontal horn diameters were 5.10 mm, the occipital horn diameters were 19 mm, and the temporal horn was 5.5 mm (5.10 ± 2.5 mm, 19 ± 5.5 mm, 5.5 ± 2.2 mm, respectively). There was no significant difference between the cases in terms of right or left comparison ($P > .05$). As a requirement of colpocephaly, occipital horns were found to be significantly higher than frontal and temporal horns (19 ± 5.5 mm vs. 5.10 ± 2.5 mm and 5.5 ± 2.2 mm, $P < .01$) (Table 1). It was found that if the occipital horn of the lateral ventricle is over 20 mm and the other horns are smaller than 7 mm, it can predict the presence of colpocephaly with a sensitivity of 94% and a specificity of 95% (area under the curve = 0.728).

MAIN POINTS

- Recognizing the lateral ventricle diameters in cases of colpocephaly facilitates diagnosis. The most important radiological finding in cases with colpocephaly is the occipital horn of the lateral ventricle greater than 20 mm. Another supporting finding in the diagnosis is the other segment measurements of the lateral ventricle less than 7 mm.
- Although the sample size of our study was not sufficient, it was larger than other similar studies. In addition, only the pediatric age group should be included in the study, which should be our goal in the next study.
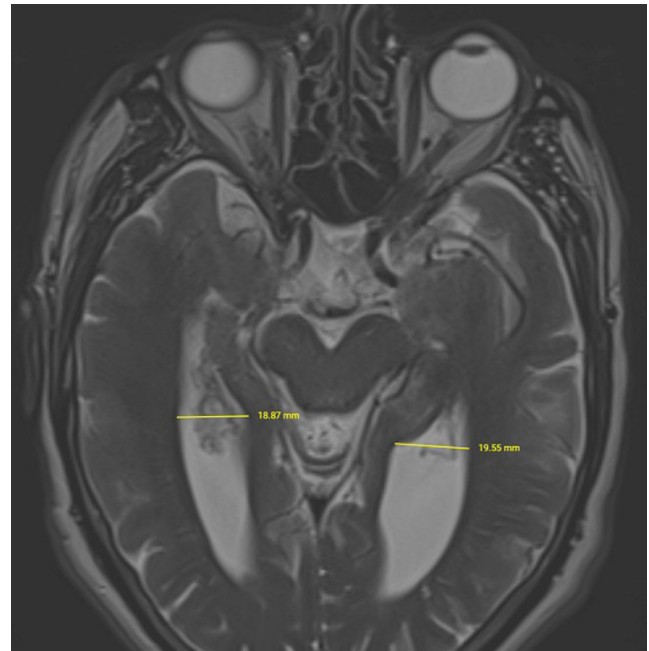

Figure 2. The measurement of the occipital horns of the lateral ventricles in a 40-year-old male patient with colpocephaly and agenesis of the corpus callosum is schematized. The measurements were 18.87 mm on the right and 19.55 on the left in both lateral ventricles.

DISCUSSION

There are just 2 other adult cases reported in medical literature, making colpocephaly a diagnosis that is well accepted in pediatrics. Benda originally identified it as a congenital type of ventriculomegaly in 1941. There were relatively few occurrences of colpocephaly that were discovered in adults, according to Srivastava et al. Esenwa and Leaf[5]

Figure 3. The measurement of the temporal horns of the lateral ventricles in a 40-year-old male patient with colpocephaly and agenesis of the corpus callosum is schematized. The measurements were 5.68 mm on the right and 5.36 on the left in both lateral ventricles.

Table 1. Diagnostic Sensitivity of LV Segment Measurements in Patients with Colpocephaly

LV Segment	Mean Diameter(mm)	P
LV frontal horn	5.10	>.05
LV temporal horn	5.50	>.05
LV occipital horn	19	<.05

LV, lateral ventricle.

described an adult patient who experienced symptoms all of her life. Asymptomatic cases of corpus callosum agenesis or dysgenesis may be diagnosed early or discovered incidentally in obstetric ultrasound scans. A rapid increase in head size due to postpartum hydrocephalus, signs of tense fontanelles, vomiting, decreased sucking, and signs of epileptic seizures may occur in severe cases.[1]

Numerous congenital insults can cause colpocephaly. It has been suggested that chromosomal anomalies, maternal toxin exposure, anoxic encephalopathy, and prenatal infections—anomalies such toxoplasmosis—are possible causes. The fetus has a stage of relative hydrocephalus just before the fifth month of life, which is typically reversed by the expansion of the surrounding white matter and corpus callosum, glial cell migration, and glioma.[6] The retained fetal ventricular shape that characterizes colpocephaly may be brought on by any intrauterine injury that hinders this maturation process.[7]

There are few studies in the literature that include occipitofrontal ratio measurement. Esenwa and Leaf[5] stated that if this ratio is above 3, it suggests colpocephaly. However, there are no studies measuring lateral ventricular diameters and normal ranges in cases of colpocephaly. In our study, the diameters of colpocephaly were measured as 5.1 mm in the frontal horn, 19 mm in the occipital horn, and 5.5 mm in the temporal horn. In this sense, it is the first study to give the mean diameters of colpocephaly. As it is known in colpocephaly, there is an increase in the occipitofrontal ratio in the lateral ventricle. In this sense, in our study, if the lateral ventricle occipital horn is larger than 20 mm and the other horns are smaller than 7 mm, it predicts colopocephaly with high sensitivity and specificity.

Adult patients were included in our study. Therefore, it is incompatible with pediatric measurements. It is recommended to determine the measurements with new studies that include pediatric subgroups in the future. Although occipitofrontal ratio measurements are available in the adult groups, they are not available in the literature in the pediatric group. Evaluation of proportional measurements together with lateral ventricular measurements in pediatric patients will increase the diagnostic quality.

There are many volumetric measurements for the lateral ventricle in the literature. However, the inclusion of volumetric measurements in cases of colpocephaly and CCA will facilitate the diagnosis in the future.

About 90 patients were included in the study, which is not sufficient. For this reason, studies with a larger population will increase reliability. Atrophic changes were not taken into account in our study. For this reason, there may have been misleading findings in the measurements. Re-evaluation with new studies and subgroups including the degree of atrophy in the future may provide high diagnostic power. The lack of proportional measurements of the lateral ventricles and the lack of volumetric calculations also reduced the diagnostic quality of our study. In addition, not using the data in tabular form in our study may cause difficulties in concentrating the attention of the readers.

Knowing the lateral ventricle diameters and using frontal and occipital threshold values together facilitate the diagnosis in cases of colpocephaly developing secondary to the corpus callosum.

CONCLUSION

REFERENCES
1. Ciurea RB, Mihailescu G, Anton RM, et al. Corpus callosum dysgenesis and colpocephaly. *Rom J Neurol*. 2013;12(3):160-163. [CrossRef]
2. Paul LK, Brown WS, Adolphs R, et al. Agenesis of the corpus callosum: genetic, developmental and functional aspects of connectivity. *Nat Rev Neurosci*. 2007;8(4):287-299. [CrossRef]
3. Keshavan MS, Diwadkar VA, Harenski K, Rosenberg DR, Sweeney JA, Pettegrew JW. Abnormalities of the corpus callosum in first episode, treatment naive schizophrenia. *J Neurol Neurosurg Psychiatry*. 2002;72(6):757-760. [CrossRef]
4. Baker LL, Barkovich AJ. The large temporal horn: MR analysis in developmental brain anomalies *versus* hydrocephalus. *AJNR Am J Neuroradiol*. 1992;13(1):115-122.
5. Esenwa CC, Leaf DE. Colpocephaly in adults. *BMJ Case Rep*. 2013. [CrossRef]
6. Puvabanditsin S, Garrow E, Ostrerov Y, Trucanu D, Ilic M, Cholenkeril JV. Colpocephaly: a case report. *Am J Perinatol*. 2006;23(5):295-297. [CrossRef]
7. Girard N, Raybaud C, Poncet M. *In vivo* MR study of brain maturation in normal fetuses. *AJNR Am J Neuroradiol*. 1995;16(2):407-413.

T2 Relaxometry in Tumefactive Demyelinating Lesions:
A Case Study

Umberto Rozzanigo[1] , Pietro Bontempi[2] , Sabrina Marangoni[3], Bruno Giometto[3] , Paolo Farace[4]

[1]Neuroradiology Hospital of Trento, Azienda Provinciale per i Servizi Sanitari, Italy
[2]Department of Computer Science, University of Verona, Verona, Italy
[3]Department of Neurology, Hospital of Trento, Azienda Provinciale per i Servizi Sanitari, Trento, Italy
[4]Department of Medical Physics, Hospital of Trento, Azienda Provinciale per i Servizi Sanitari, Trento, Italy

Abstract

Objective: The study aimed to characterize tumefactive demyelinating lesions by magnetic resonance imaging multicomponent T2 relaxation.
Methods: Quantitative T2 mapping of the intra/extra-cellular water was compared with conventional T2-weighted Fluid-Attenuated Inversion Recovery (FLAIR) and contrast-enhancement T1-weighted imaging.
Results: Tumefactive demyelinating lesions showed typical open-ring-like contrast enhancement, with no T2 hypointense rim on both FLAIR and T2-weighted but a clear heterogeneity in the intra/extra-cellular water maps. The intra/extra-cellular water T2 mapping showed a rim of shorter T2 in the same area of ring enhancement and a longer T2 in the central portion of the lesion.
Conclusions: Intra/extra-cellular water T2 mapping has a unique potential to evidence heterogeneity features and a rim of shorter T2 in tumefactive demyelinating lesion and deserves to be further investigated.
Keywords: Quantitative MRI, T2 lesions, multiple sclerosis, MRI

INTRODUCTION

Tumefactive multiple sclerosis or tumefactive demyelinating lesion (TDL) is one of the variants of multiple sclerosis (MS) and is the consequence of central nervous system idiopathic inflammatory demyelinating diseases.[1] Tumefactive demyelinating lesions are not a rare occurrence with a prevalence in the range of 1.4%-8.2% of MS patients.[2] The radiological presentation of patients with TDL is variable and atypical for demyelinating disease due to the differences in size and location of the lesion. Tumefactive demyelinating lesions can be a challenging scenario for clinicians due to difficulties distinguishing them from other conditions, such as neoplasm or infection, and because they can be caused by a heterogeneous range of disorders.[1-3]

Magnetic resonance imaging (MRI) characterization of the myelin component can provide information on demyelinating diseases, offering greater insight into MS-driven pathology and its clinical manifestations.[4] To date, several techniques have been identified and one of the methods is based on the analysis of the transverse relaxation times (T2) of the axonal tissue, with multi-echo sequences and multi-exponential analysis (T2 relaxation). The multi-component nature of the white matter has been established, attributing to each component a different T2, of which at least 1 component is due to water trapped in the myelin lipid membrane and the other to the intra/extra-cellular water.[5] The application of multi-component T2 relaxometry in MS has been mainly focused on the myelin water pool, that is, myelin water fraction, and the intra/extra-cellular water (IEw) was only occasionally investigated in diffusely abnormal white matter.[6]

Herein, we describe a case of TDLs assessed for the first time by IEwT2 relaxation, combined with conventional FLAIR, T2-weighted, and post-contrast T$_1$-weighted MRI. We aimed to investigate whether IEwT2 can provide additional information, especially concerning TDL heterogeneity.

CASE PRESENTATION

A 44-year-old female, affected by relapsing-remitting MS, was recruited from an institutional review board-approved study on the application of T2 relaxometry in MS. The patient had disease onset at the age of 28, with clinical relapses at ages 30 and 31, when she started treatment with a first-line disease-modifying therapy (DMT) until the age of 42 when she experienced clinical relapse with Expanded Disability Status Scale (EDSS) of 2.5. After steroid treatment with benefit, the patient changed therapy with fingolimod (approved as second-line DMT in Europe). The patient was fine until she presented relapse with EDSS 3.5 and underwent the MR examination described in the following.
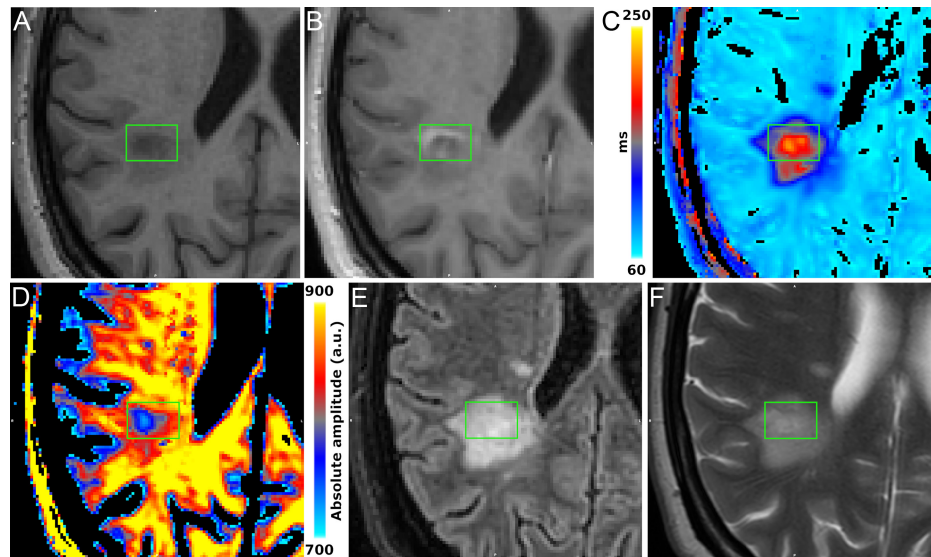
Figure 1. From top to bottom: T1-weighted images (pre- and post- contrast enhancement), maps of the intra-extracellular water component (IEwT2 map on the left and the corresponding amplitude on the right), T1-weighted images (FLAIR on the left and T2-image on the right). The green rectangular contour identifies the same region on all the different images/maps. IEwT2, T2 mapping of the intra/extra-cellular water.

The patient underwent conventional MRI, including FLAIR, T2-weighted, and pre- and post-contrast T1-weighted sequences. Additionally, multi-component T2 relaxation was performed by a multi-echo sequence with 32 equally spaced echoes (10-320 ms). The T2 decay signal was decomposed into 3 main components: myelin water below 40 ms, intra-extracellular water (IEw) between 40 and 250 ms, and free water above 250 ms. The obtained IEwT2 mapping was compared with conventional T2, FLAIR, and T1 imaging. Two active TDLs plaques were identified (Figures 1 and 2), showing open-ring contrast enhancement, with no T2 hypointense rim on both FLAIR and T2-weighted images, which resulted in homogeneous hyperintensity, but a clear heterogeneous pattern in the IEw maps. The IEwT2 showed a rim of shorter T2 in the same area of ring enhancement and a longer

T2 in the central portion of the TDLs. Finally, in the 2 TDLs, quantitative IEwT2 showed a T2 that increases with the size of the lesion.

DISCUSSION

Pseudotumoral TDLs occur in MS and related diseases and are considered an atypical manifestation of central nervous system demyelination. Lesions are called "pseudotumoral" as they may be mistaken for neoplasm, leading to morbidity from brain biopsy and other procedures, delays in appropriate treatment, and unnecessary anguish for patients.[2] Although some radiological characteristics can help make a differential diagnosis easier, a cerebral biopsy may still be necessary. Helpful MRI characteristics that favor a tumefactive demyelinating lesion include size, surrounding edema, a T2 hypointense rim,
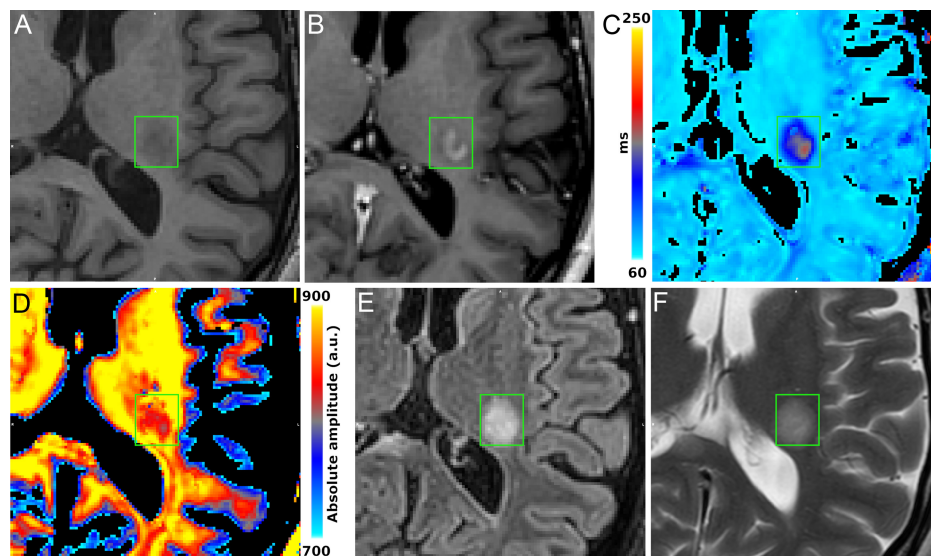

Figure 2. From top to bottom: T1-weighted images (pre- and post- contrast enhancement), maps of the intra-extracellular water component (IEwT2 map on the left and the corresponding amplitude on the right), T1-weighted images (FLAIR on the left and T2-image on the right). The green rectangular contour identifies the same region on all the different images/maps. IEwT2, T2 mapping of the intra/extra-cellular water.

open-ring enhancement, and the presence of other more typical MS demyelinating lesions elsewhere on the MRI.[2]

Contrast enhancement shaped as an open ring or a crescent circumscribed to the white matter is considered a specific neuroimaging sign for differential diagnosis and distinguishing demyelinating lesions from neoplasms and infections.[7] Furthermore, the presence of a T2 hypointense ring around the lesion is also a feature that may point toward the diagnosis.[3] Such T2 hypointense rim is often present in the same area of ring enhancement with the majority of lesions showing some degree of associated T1 hypointensity.[1] Hypointense T2 rims have also been associated with non-tumefactive ring-enhancing MS lesions.[8] In a study of 54 patients presenting radiographically with TDL (1 of the largest published cohorts of patients), 42% showed a T2 hypointense rim.[9] Moreover, in the patients with a tumefactive onset, the absence of a T2 hypointense rim resulted in an appreciably (although not significant) longer conversion time to MS compared to the patients with a T2 hypointense rim. In that study, no other radiological characteristics of TDLs had any correlation with conversion to MS.[11]

In the reported case, no clear T2 hypointense ring was visible on both FLAIR and T2-weighted images in 2 TDLs, while IEwT2 evidenced a clear heterogeneous pattern, with a rim characterized by a shorter T2. In a recent study, quantitative IEwT2 mapping resulted in higher sensitivity than conventional FLAIR to detect subtle brain tissue alterations,[10] suggesting that current T2 relaxometry, at the price of lower spatial resolution, can offer improved T2 resolution than FLAIR. The reported case demonstrated that IEwT2 can also provide more information than conventional T2 imaging, due to the intrinsic discrimination between the amplitude and the T2 decay of the signal, allowing much better detection of T2 lesion heterogeneity. This unique potential deserves to be further investigated in TDLs and in other ring-enhancing and/or heterogenic MS lesions.

Informed Consent: Written informed consent was obtained for the participant

REFERENCES

1. Algahtani H, Shirah B, Alassiri A. Tumefactive demyelinating lesions: a comprehensive review. *Mult Scler Relat Disord*. 2017;14:72-79. [CrossRef]
2. Hardy TA. Pseudotumoral demyelinating lesions: diagnostic approach and long-term outcome. *Curr Opin Neurol*. 2019;32(3):467-474. [CrossRef]
3. Frederick MC, Cameron MH. Tumefactive demyelinating lesions in multiple sclerosis and associated disorders. *Curr Neurol Neurosci Rep*. 2016;16(3):26. [CrossRef]
4. Edwards EM, Wu W, Fritz NE. Using myelin water imaging to link underlying pathology to clinical function in multiple sclerosis: A scoping review. *Mult Scler Relat Disord*. 2022;59:103646. [CrossRef]
5. MacKay AL, Laule C. Magnetic resonance of myelin water: an in vivo marker for myelin. *Brain Plast*. 2016;2(1):71-91. [CrossRef]
6. Papadaki E, Mastorodemos V, Panou T, et al. T2 relaxometry evidence of microstructural changes in diffusely abnormal white matter in relapsing-remitting multiple sclerosis and clinically isolated syndrome: impact on visuomotor performance *J Magn Reson Imaging*. 2021;54(4):1077-1087. [CrossRef]
7. Masdeu JC, Quinto C, Olivera C, Tenner M, Leslie D, Visintainer P. Open-ring imaging sign: highly specific for atypical brain demyelination. *Neurology*. 2000;54(7):1427-1433. [CrossRef]
8. Llufriu S, Pujol T, Blanco Y, et al. T2 hypointense rims and ring-enhancing lesions in MS. *Mult Scler*. 2010;16(11):1317-1325. [CrossRef]
9. Altintas A, Petek B, Isik N, et al. Clinical and radiological characteristics of tumefactive demyelinating lesions: follow-up study. *Mult Scler*. 2012;18(10):1448-1453. [CrossRef]
10. Bontempi P, Rozzanigo U, Amelio D, Scartoni D, Amichetti M, Farace P. Quantitative multicomponent T2 relaxation showed greater sensitivity than FLAIR imaging to detect subtle alterations at the periphery of lower grade gliomas. *Front Oncol*. 2021;11:651137. [CrossRef]

Magnetic Resonance Imaging Findings of Bilateral Asymmetrical Involvement of Brucella Sacroiliitis

Volkan Kızılgöz

Department of Radiology, Erzincan Binali Yıldırım University, Faculty of Medicine, Erzincan, Turkey

Abstract

Brucellosis is a zoonosis that may affect various organs or systems. The musculoskeletal system is the most commonly affected site in human brucellosis. Brucellosis usually presents with unilateral involvement in sacroiliac joints. Herein, a case of bilateral asymmetric involvement of brucellosis in both sacroiliac joints is presented with magnetic resonance imaging findings.

Keywords: Brucellosis, magnetic resonance imaging, sacroiliitis, sacroiliac joint

INTRODUCTION

Human brucellosis remains a significant public health problem in most developing countries. The musculoskeletal system is one of the most common sites affected by this zoonosis and affects 20%-40% of the patients with brucellosis.[1] Vertebral osteomyelitis related to brucellosis is commonly encountered in Mediterranean countries.[2] Moreover, the sacroiliac joint is the most commonly reported osteoarticular space in the literature for this disease.[3] Sacroiliitis is defined as the inflammation of the sacroiliac joint or both sacroiliac joints, and this entity may have an acute or chronic presentation. The chronic presentation can usually be underlaid by rheumatic inflammatory and non-inflammatory diseases. Acute sacroiliitis is rare and is more likely caused by infectious or neoplastic processes.[4,5] Patients may present with severe pain because of nerve irritations, due to the adjacent lumbosacral plexus, mainly due to the involvement of L4-L5 nerves.[6] Magnetic resonance imaging (MRI) is a very useful imaging technique to detect the involvement of brucellosis in sacroiliac joints. The typical involvement pattern of brucella sacroiliitis is unilateral, and the aim of this article is to present the bilateral asymmetric involvement of brucellosis in sacroiliac joints.

CASE REPORT

After obtaining the consent form from the patient, the history and laboratory results were noted, and MR images were obtained using the picture archiving and communication system to prepare this article.
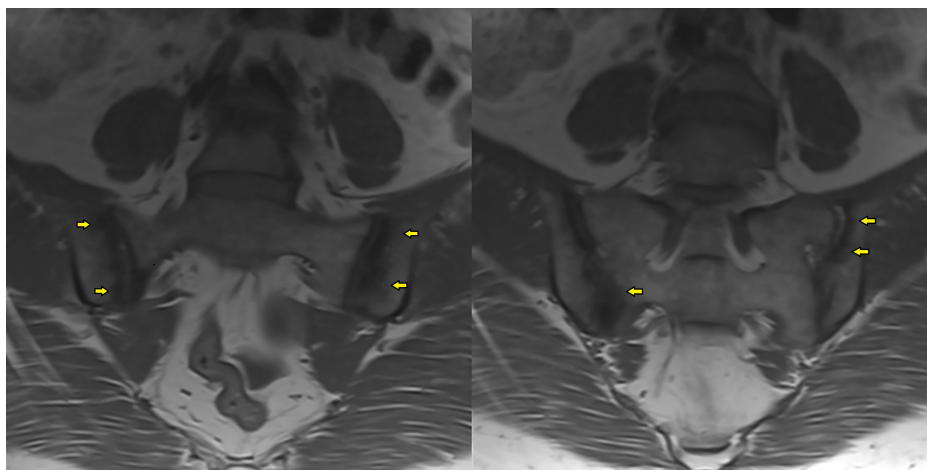

Figure 1. T1-weighted coronal plane images indicate bilateral subchondral sclerosis with hypointense signal in both sacroiliac joints (yellow arrows show the hypointensity representing subchondral sclerosis).
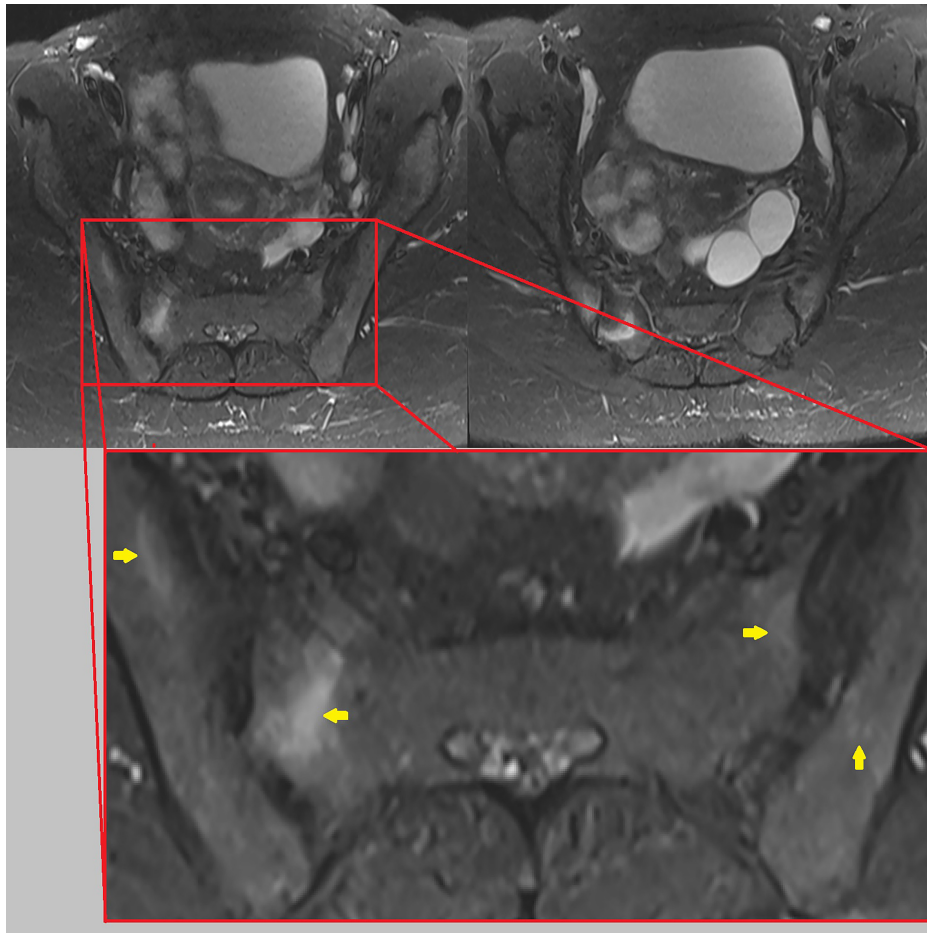
Figure 2. T2-weighted axial plane short tau inversion recovery (STIR) images reveal the subchondral and medullar edema in both sacroiliac joints with right-sided dominance, and the yellow arrows point to areas of bone marrow edema in the magnified image.

A 46-year-old female patent was admitted to the physical therapy and rehabilitation department complaining of lower back and right flank pain. The patient was living in a rural area, and she was a farmer. She did not have any history of psoriasis, urethritis, diarrhea, trauma, or familial inflammatory arthropathy. Her temperature, blood pressure, and heart rate were normal. Her leukocyte count was 6900/µL, sedimentation rate was 46 mm/h, and C-reactive protein level was 94.8 mg/dL. Alanine transaminase, aspartate transaminase values, serum calcium, uric acid results, and urine test results were within normal limits. There was no positive result for a purified protein derivative (PPD) test for tuberculosis and the results of the other rheumatological laboratory tests were negative. Brucella Rose Bengal test was positive, and the Brucella immunocapture test was positive for 1/320 titer. She was then consulted with the infectious diseases department, and the clinicians requested a sacroiliac MRI.

MAIN POINTS

- Psoriatic arthritis, gout, or reactive arthritis are usually encountered with bilateral asymmetrical involvement.
- Enteropathic arthritis, ankylosing spondylitis, and rheumatoid arthritis tend to present with bilateral and symmetric sacroiliitis.
- Pyogenic septic arthritis, tuberculous sacroiliitis, and brucella sacroiliitis are usually observed with unilateral involvement.

Sacroiliac MR images revealed bilateral subchondral sclerosis (low signal on T1W and T2W images) (Figure 1) and bone marrow edema (low signal on T1W images and high signal on T2W images, especially on T2W short tau inversion recovery (STIR) images) in ilium and sacrum (Figure 2). There were patchy contrast-enhanced areas in the joints' iliac and sacral sides. The distribution of MRI findings showed right-sided and sacral dominance (Figure 3). An obvious periarticular involvement had not been indicated; however, MRI revealed high signals in the superior intraarticular space of the right sacroiliac joint on the T2-weighted fat-saturated coronal plane which might represent a small amount of intraarticular fluid accumulation with chondral edema (Figure 3C).

DISCUSSION

Brucellosis is a well-known zoonosis caused mainly by animal contact or consumption of unpasteurized milk. Patients generally present with undulating fever. Myalgia, arthralgia, and back pain are other common complaints and symptoms of this disease. Blood tests should be done to confirm the diagnosis. Brucellosis may present with hepatomegaly, splenomegaly, or lymphadenopathy, but none of them are characteristic of this disease that affects various organs and tissues.

Brucella spondylodiscitis constitutes 6%-58% of all brucellosis osteo-articular involvements. The most affected areas in the spinal system are as follows: the lumbar area (60%), thoracic area (19%), and cervical
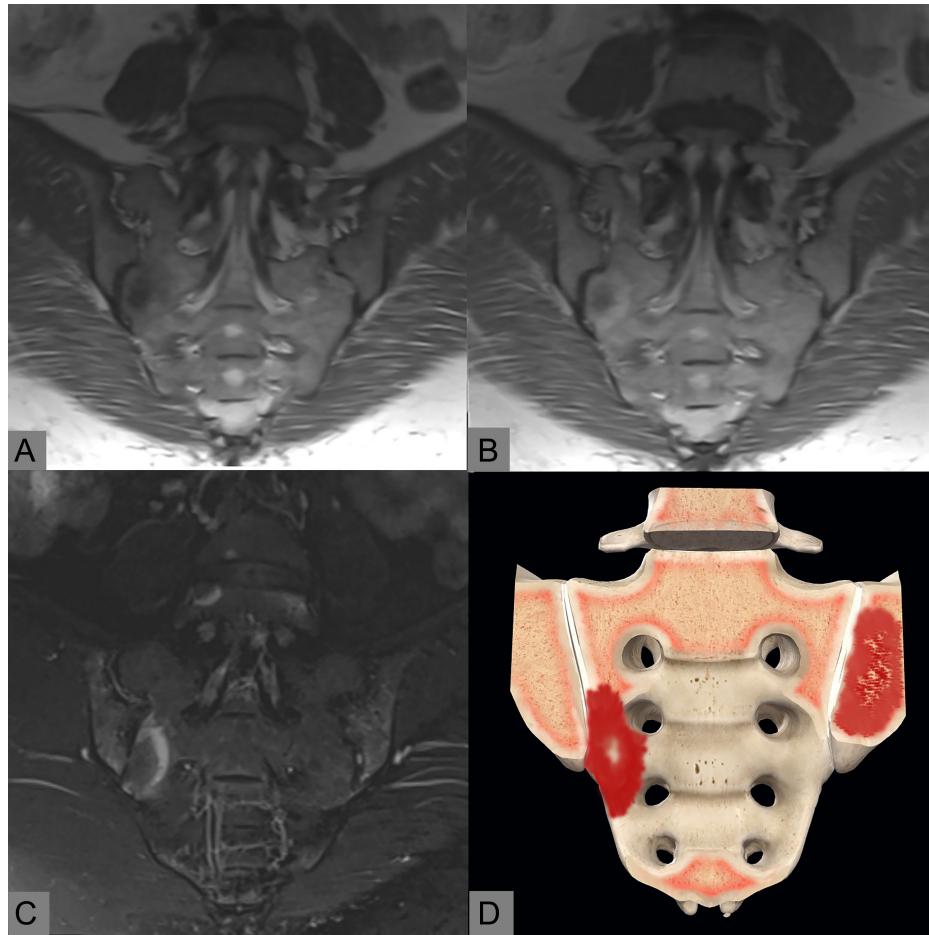
Figure 3. T1-weighted (A), contrast-enhanced T1-weighted (B), and T2-weighted fat-saturated (C) coronal plane images indicate the asymmetric bilateral sacroiliac involvement of the disease. Three-dimensioanal schematic image depicts the subchondral and medullar edema of the sacroiliitis (D).

area (12%).[7] Unilateral sacroiliitis is the most common form of sacroiliitis in brucellosis. However, asymmetric bilateral involvement may also be encountered.[8]

Especially in the early stages, plain radiography has a limited role in diagnosing sacroiliitis due to the poor sensitivity of this imaging technique. However, conventional x-rays are still used as the initial imaging method. Computed tomography has higher sensitivity than radiography for detecting joint space narrowing and millimetric bony erosions.[9]

Magnetic resonance imaging, with the absence of ionizing radiation, has the advantage to reveal the early involvement and is still the imaging method of choice for sacroiliitis. Bone marrow edema in subchondral areas is characterized by low T1 and high T2 signals. As a very sensitive MRI sequence for bone marrow edema, the STIR sequence is also helpful in determining edema in the early stages of the disease. Contrast-enhanced T1-weighted fat-saturated images are also valuable for detecting active disease in sacroiliitis. T2-weighted imaging and STIR sequences are very helpful to show intraarticular fluid collection; moreover, bony erosions can also be depicted using MRI. Imaging periarticular soft tissue involvement is another advantage of MRI as this technique has the superiority to revealing the extent of sacroiliitis to muscle and other periarticular soft tissues. This modality will

also reveal subchondral sclerosis, bony erosions, and ankylosis in the chronic phase of the infection.[10]

Involvement of sacroiliitis by various diseases can be classified concerning bilateral–unilateral or symmetrical–asymmetrical involvement of the disease. Psoriatic arthritis, gout, or reactive arthritis are usually encountered with bilateral asymmetrical involvement. Enteropathic arthritis, ankylosing spondylitis, and rheumatoid arthritis tend to present with bilateral and symmetric sacroiliitis. Pyogenic septic arthritis, tuberculous sacroiliitis, and brucella sacroiliitis are usually observed with unilateral involvement. In this current case report, we presented a case of brucellosis with bilateral asymmetrical involvement of sacroiliac joints.

Besides various infectious and rheumatological diseases, which may involve the sacroiliac joints, metastatic lesions, destructive neoplastic processes, hyperparathyroidism, and osteitis condensans ilii may also mimic sacroiliitis and should be kept in mind for the differential diagnosis of sacroiliitis.[11]

Informed Consent: Written informed consent was obtained from the patient who participated in this case report.

Peer-review: Externally peer-reviewed.

Declaration of Interests: The authors declare that they have no competing interest.

REFERENCES

1. Mehanic S, Baljic R, Mulabdic V, et al. Osteoarticular manifestations of brucellosis. *Med Arch*. 2012;66(3):24-26. **[CrossRef]**
2. Rubach MP, Halliday JE, Cleaveland S, Crump JA. Brucellosis in low-income and middle-income countries. *Curr Opin Infect Dis*. 2013;26(5):404-412. **[CrossRef]**
3. Antonelli MJ, Magrey M. Sacroiliitis mimics: a case report and review of the literature. *BMC Musculoskelet Disord*. 2017;18(1):170. **[CrossRef]**
4. Slobodin G, Hussein H, Rosner I, Eshed I. Sacroiliitis – early diagnosis is key. *J Inflamm Res*. 2018;11:339-344. **[CrossRef]**
5. Navallas M, Ares J, Beltrán B, Lisbona MP, Maymó J, Solano A. Sacroiliitis associated with axial spondyloarthropathy: new concepts and latest trends. *RadioGraphics*. 2013;33(4):933-956. **[CrossRef]**
6. Karami MM, Al-Mufarrh DS. Acute Pyogenic Sacroiliitis: Brucellosis and early diagnosis. *Egypt J Hosp Med*. 2021;85(1):2785-2787. **[CrossRef]**
7. Korkmaz P, Ataizi ZS, Çevik FG, et al. Brucella spondylodiscitis: Multifocal involvement in thoracic and lumbar areas; a rare case. *J Microbiol Infect Dis*. 2015;5(3):129-132. **[CrossRef]**
8. Özeri Z, Nacır B, Çakıt BD, Saraçoğlu M, Erdem HR. Fırat tıp. *Dergisi*. 2010;15(1):44-47.
9. Arkun R, Mete BD. Musculoskeletal brucellosis. *Semin Musculoskelet Radiol*. 2011;15(5):470-479. **[CrossRef]**
10. Bozgeyik Z, Aglamis S, Bozdag PG, Denk A. Magnetic resonance imaging findings of musculoskeletal brucellosis. *Clin Imaging*. 2014;38(5):719-723. **[CrossRef]**
11. Alp E, Doganay M. Current therapeutic strategy in spinal brucellosis. *Int J Infect Dis*. 2008;12(6):573-577. **[CrossRef]**

Acknowledgement of Reviewers

Ahmet Gürkan Erdemir	Emre Mircik	Nesrin Ceylan
Baki Hekimoğlu	Fatma Dilek Gökharman	Oğuzhan Tokur
Barış Irgulas	Hasan Aydın	Okan Dilek
Berna Uçan	Hasan Yiğit	Ömer Kaya
Burçak Çakır Peköz	İbrahim Feyyaz Naldemir	Özlem Aydın
Bünyamin Ece	Leyla Karaca	Selma Uysal Ramadan
Çiğdem Üner	Maksude Esra Kadıoğlu	Tümay Bekçi
Düzgün Can Şenbil	Mesut Özgökçe	Viswanathan Padmanabhan
Eda Beykoz Çetin	Mesut Öztürk	Volkan Kızılgöz